

Review

First-Principles View on Photoelectrochemistry: Water-Splitting as Case Study

Anders Hellman * and Baochang Wang

Competence Centre for Catalysis and the Department of Physics, Chalmers University of Technology, 412 96 Gothenburg, Sweden; Baochang@chalmers.se

* Correspondence: anders.hellman@chalmers.se; Tel.: +46-31-72386-9804

Academic Editor: Matthias Bauer

Received: 30 March 2017; Accepted: 24 May 2017; Published: 1 June 2017

Abstract: Photoelectrochemistry is truly an interdisciplinary field; a natural nexus between chemistry and physics. In short, photoelectrochemistry can be divided into three sub-processes, namely (i) the creation of electron-hole pairs by light absorption; (ii) separation/transport on the charge carriers and finally (iii) the water splitting reaction. The challenge is to understand all three processes on a microscopic scale and, perhaps even more importantly, how to combine the processes in an optimal way. This review will highlight some first-principles insights to the above sub-processes, in particular as they occur using metal oxides. Based on these insights, challenges and future directions of first-principles methods in the field of photoelectrochemistry will be discussed.

Keywords: water splitting; photoelectrochemistry; first-principles

1. Introduction

“Water will be the coal of the future” states Cyrus Harding, one of the protagonists in Jules Verne’s novel “The Mysterious Island” [1]. Interestingly this is the conclusion after the protagonists have discussed the fact that the known coal reserves will eventually be depleted. The analogy to today’s crude oil is obvious. Based on the simple fact that it takes millions of years to produce fossil fuel, whereas the extraction, in comparison, is very fast, the depletion of crude oil is certain [2–4], although the exact time remains debatable.

The scenario of depleting crude oil reserves is in stark contrast to the increase in global energy consumption. In 2015, the global power consumption was estimated to be a total of 17 TW [5], and projections for 2050 ranges between 28 and 31 TW [6,7]. This increased demand of energy is known as the TW challenge [8–10], and alternative energy solutions must be able to contribute to the TW level in order to make an appreciable impact at a global scale [11,12].

In light of possible peak oil production, increased global energy consumption and humanity’s environmental footprint, we need to find a renewable source of energy that enables us to move away from fossil fuels. An obvious candidate is the Sun. For instance, more energy from sunlight strikes Earth in one hour than what society currently consumes in a year [13]; thus the Sun easily rises to the TW challenge. Solar energy can be harvested in many different ways [14–17]. For instance, photosynthesis, which plays a crucial role for life on Earth, is able to transform sunlight to chemical energy in the form of biomass. If the biomass is produced from plants with low water and fertilizer requirements, and without competition with ordinary food production, then biomass can contribute to the TW challenge by e.g., use of conventional thermal power plants. Other conventional methods like wind and wave power, which is an indirect form of solar energy, can generate electricity, which is also true for photovoltaic cells. Today, silicon based solar cells have an energy conversion efficiencies of approximately 15% to 25% [18], but there exist several of similar techniques. For instance, aqueous dye-sensitized solar cells (DSSCs) work as an artificial photosynthetic system converting solar energy

into electricity, and have recently emerged as an alternative to silicon-based solar cells owing to the low cost, synthetic flexibility, ease of fabrication, and short energy payback time. Moreover, the conversion efficiencies have recently exceeded 14% [19]. The most recent studies on such systems can be found in Ref. [18,20–22]. Yet another method to utilize the energy of sunlight is to use the energy to break chemical bonds, thereby storing energy in a chemical form. This is the basic challenge in water-splitting, i.e., with the help of sunlight split water into hydrogen and oxygen [23–25]. Cyrus Harding explains to his fellow castaways “water will one day be employed as fuel, that hydrogen and oxygen which constitute it, used singly or together, will furnish an inexhaustible source of heat and light, of an intensity of which coal is not capable” [1]. In case of photocatalysis, a photocatalyst is used to capture photons with higher energies than the band gap of the material, i.e., excite electrons from valence band to conduction band [26–30]. These photogenerated carriers can participate the reduction and oxidation reactions of water to hydrogen and oxygen. In order to achieve this, the band positions of the photocatalyst must lie on both sides of the reduction and oxidation potentials of water. In the case of photoelectrochemistry [23–25] the electrochemical setup provide the possibility of applying an external potential that can further assist in the overall reaction, i.e., provide additional driving force to the photogenerated carriers to split water.

In 1972, Honda-Fujishima published a ground-breaking study in which hydrogen was produced from water using TiO_2 as the photoanode material [31], proving that it is indeed possible to do photoelectrochemical water splitting. A schematic energy diagram of the basic principles of water splitting by a photoelectrochemical cell using a photoanode (photoactive semiconductor material) for the oxygen evolution reaction (OER) and a cathode for the hydrogen evolution reaction (HER) is shown in Figure 1. When light interacts with the photoanode, the electrons in the valence band have the possibility to cross the forbidden band-gap and, thus, be excited into the conduction band while the holes remain in the valence band. The holes will move towards the interface of the photoanode and electrolyte where they will participate in the water splitting, while the electrons will move to the cathode side and participate in the HER. The free energy change in the water splitting reaction ($2\text{H}_2\text{O} \rightarrow 2\text{H}_2 + \text{O}_2$) amounts to 4.92 eV, which in a four-electron process implies that each electron-hole needs to bring 1.23 eV to the reaction. Hence, the photoanode material must absorb light to make its electrode potential higher than 1.23 V, which puts a lower bound on the band-gap. There exist several of excellent textbooks [32–34] and reviews [23,35–39] describing the above process in detail.

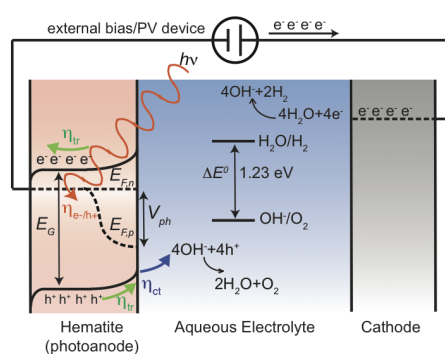


Figure 1. A schematic energy diagram for a photoanode (n-type semiconductor). Several important steps are illustrated, namely: (i) light absorption η_{e^-/h^+} ; (ii) charge transport η_{tr} ; and (iii) surface chemical reactions η_{ct} . Photons with energy equal to or larger than the band-gap E_g are absorbed with efficiency η_{e^-/h^+} . The built-in electric field drives holes towards the photoanode/electrolyte interface and electrons to the cathode (usually via a charge collector and an external circuit). η_{tr} is the fraction of photogenerated charges reaching the respective solid/liquid interface. Holes are transferred to the electrolyte with efficiency η_{ct} and take part in the oxygen evolution reaction (OER). An external bias/PV device supplies electrons with sufficient energy so that they take part in the hydrogen evolution reaction (HER). Reproduced with permission from ref. [40], published by The Royal Society of Chemistry.

Therefore, what are the criteria that an ideal photoanode material needs to fulfill? Simply put, there are five criteria: (1) by necessity, the band-gap must be larger than 1.23 eV, however, with respect to energy losses, a more practical band-gap is around 2.0 eV, which still allows the photoanode to be working under visible light as half of the incoming solar energy comes from visible light and shorter wavelengths; (2) band edge positions should straddle the redox potentials of water; (3) electron-hole mobility and lifetime that allow the electron-hole pair to reach the active sites, e.g., materials with few defects and small particle size inhibit electron-hole recombination; (4) the rate of oxygen evolution reaction must be larger than any competing recombination reaction where the activity and the number of active sites become crucial; (5) the material needs to be stable in an aqueous environment and under illuminating conditions i.e., to avoid anion from the catalyst itself being oxidized by photogenerated holes instead of water. However, in practice, the performance gap exists between a real photoanode and an ideal photoanode shown in Figure 2. The main performance limiting factors for increasing anodic potential are indicated by arrows. Although, there exist promising candidates, such as tungsten oxide and hematite, the challenge to find one such material remains to be solved [41]. For instance, owing to the relatively large band-gap (3.2 eV) of TiO_2 [42], only a fraction of the solar spectrum is utilized, which ultimately puts some hard limitation of the use of TiO_2 to resolve the TW challenge [35].

Density functional theory (DFT) is based on two theorems [43] that in principle are a recast of the Schrödinger equation into a functional form and instead of dealing with the many-body wave-function focus on the density. Several excellent reviews [44,45] and textbooks [46–48] discuss the fundamentals of DFT, and a brief discussion on the methodologies of DFT are provided in the appendix part of this paper. Being a first-principles method, DFT is able to predict many properties of any atomic system, and there exist several of successful examples in the literature. In the last decade, the predictive power of first-principles has been used in high-throughput computational materials studies [49,50]. With the historical increase in available computer power, it is clear that first-principles will become the first starting point when a new material property is desired or even when an unknown material is needed.

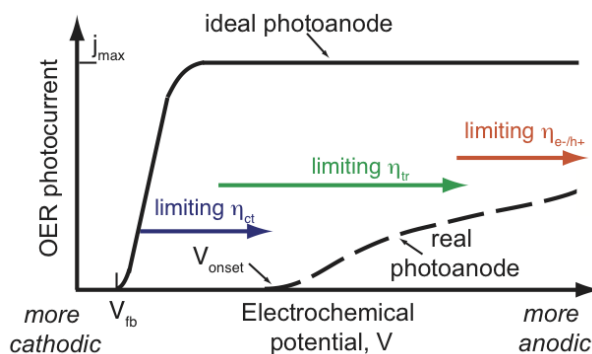


Figure 2. PEC performance gap between a state-of-the-art photoanode and the ideal photoanode. The arrows indicate the main performance limiting factors for increasingly anodic potential: first charge transfer at the photoanode/electrolyte interface and the small photovoltage, then charge transport within photoanode and finally light absorption in the semiconductor. Reproduced with permission from ref. [40], published by The Royal Society of Chemistry.

This review focus on how first-principles methods can address the processes involved in photoelectrochemistry, namely photoexcitation of electron-hole pairs, separation and transport of the holes to the semiconductor/electrolyte interface where the oxygen evolution reaction takes place. The hope is that by providing further understanding of the underlying mechanisms, this will assist in the development of new or improved photoanode materials. This review is far from complete, and some aspects will not get the attention they deserve, for which the authors can only apologize. In more specific terms, only a limited number of first-principles studies of how dopants affect light absorption, carrier transport, and catalytic reactions are included, although the study of dopants are the

bread-and-butter of first-principles. Further, the focus is on standard DFT, and only briefly are results from time-dependent DFT and molecular dynamics accounted for. In addition, experimental literature is not discussed in-depth. These limitations are not because these aspects are not important. On the contrary, all of them deserve their own extensive review. However, to make this review tractable these limitations are included nonetheless.

2. Processes Involved in Photoelectrochemistry

There are many microscopic processes involved in photoelectrochemistry, such as light-matter interaction, transport phenomena, charge-transfer reactions, solid-liquid interaction, and many more. In an attempt to provide an overview of the processes involved and how to tackle them with first-principles methods, we will limit ourselves to three separate major processes. These will be (i) creation of electron-hole pairs, (ii) charge carrier transport and (iii) electrochemical surface reactions.

2.1. Creation of Electron-Hole Pairs

As light penetrates the photo-active semiconductor, the electronic structure of the material will interact with the propagating electromagnetic wave [51,52]. The interaction might result in an electronic excitation where an electron in an occupied band is transferred to an unoccupied band. In the case of a semiconductor, the occupied (valance) band and unoccupied (conduction) band is separated by a band-gap. The band-gap efficiently hinders the dissipation of energy, as the lack of accessible electronic states quenches many of the common dissipation channels (carrier-carrier interaction and the phonon coupling) [51]. Generally, one can classify band-gaps into two classes: direct and indirect band-gaps. The difference lies in the prerequisite for the photon adsorption. In the case of a direct band-gap, the electron can transfer to the conduction band without any change in its momentum, whereas in the case of an indirect band-gap, the transfer also requires the creation/annihilation of one (or many) lattice phonon(s), which makes the probability for this process much less as compared to the probability in a direct band-gap.

It is, of course, possible to transfer electrons deeper down in the valance band and/or to higher states in the conduction band if the photon energy is larger than the band-gap. These electron-hole pairs are in a non-equilibrium state, but thanks to carrier-carrier interaction and phonon coupling, the additional energy is quickly dissipated. The cooling process normally goes through the following steps [53–55]; first, the electron and the hole reach equilibrium by their respective carrier-carrier collisions, resulting in two different temperatures defined by the distribution of energy of the respective carrier distribution. This temperature is always higher than the phonon temperature, thereby giving rise to the terms hot electrons and hot holes. This relaxation process is very rapid (1–10 fs). Second, the hot carriers are equilibrating with the phonons, through carrier-phonon interactions thereby transferring excess energy to the heating of the photoanode material. The relaxation process occurs on the time scale of 1–100 ps. The last step involves the electron-hole recombination, either radiatively (luminescence) or nonradiatively (heat). A schematic of these processes is shown in Figure 3. Assuming that the above dissipation channels are efficient, the theoretical power conversion of a photo-active semiconductor depends only on the band-gap and the incident light spectrum [42]. Although there exists ways to modify the solar spectra, for instance combining low-energy photons to create a higher energy photon (photon fussion) [56], the most obvious parameter to optimize is the band-gap.

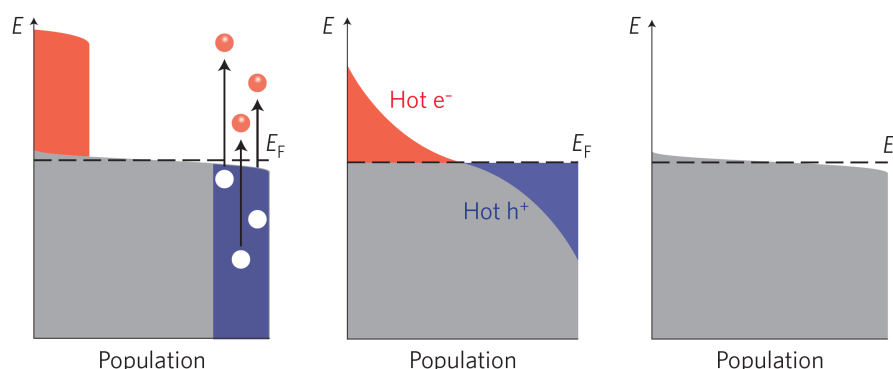


Figure 3. The relaxation process of hot electron-hole pairs. There exist several pathways for dissipation of the energy of the electron-hole pairs. More details of these are given in the text. Reprinted by permission from Nature Nanotechnology, copyright 2015 [54].

DFT is a proven method, able to explain, predict and guide experimental results; however, in the case of band-gap design, there is a well-known problem. The most frequently-used approximations for the exchange-correlation functional simply fails at calculating the band-gap of even the simplest materials. For instance, Si is calculated to have a band-gap of 0.52 eV, whereas the experimental value is 1.17 eV [57,58]. There are many extensions to circumvent this problem, such as, DFT + U, hybrid functionals and random-phase approximation [59]. However, there is also work being done on the simple semi-local functionals; see for instance [60,61], which describe PBEsol and GLLB-SC. The latter has recently been compared to more advanced methods, in this case GW [62], with very good agreement [63]. Using the GLLB-SC has allowed the use of high-throughput screening [63] and machine-learning techniques [64] to find materials with suitable band-gaps for water-splitting.

The fundamental and optical band-gap of semiconductors can be modified not only by changing material properties (structure, composition, etc.), but also through doping. The description of dopants in semiconductors using DFT requires accurate description of the band structure and the charge states of transition levels [65]. The defect energy levels can be described with the obtained single-particle Kohn-Sham eigenvalues, while determining the transition between different charge states can be evaluated using the approach described by Lany and Zunger [66] or Van de Valle and Neugebauer [67]. However, the well-known band gap problem and the insufficient cancellation of the self-interaction energy are the two main drawbacks of DFT [68]. DFT + U or hybrid functionals represents a general and practical solution to the problems, although limited by offhand parameters, such as, the U value in DFT + U or the fractional of exact Hartree-Fock exchange in hybrid functionals [69–72]. Technically, when modeling doped systems, corrections of finite-size effects are required in supercell calculations, especially in the case of charged defects [73] or when Moss-Burstein-type band-filling effects are important [74,75]. Many approaches and schemes have been applied to address this, readers are referred to Ref. [66] and references therein for details. Dopant can either stay at interstitial site or substitute one of the host atom in bulk materials depending on the magnitude of the formation energy of different configurations, which can be calculated using DFT. In cubic system, the lattice parameters are often linearly dependent on the dopant concentration following the empirical Vegard law [76–78]. For other systems, equilibrium volume can be obtained by fitting the DFT calculated energies to the Birch–Murnaghan equation of states [79,80]. There exist numerous examples from the literature where first-principles have been used to guide which doped atoms to use to improve the band-gap of a given material. For instance, Asahi et al. [81,82] showed that nitrogen doped into substitutional sites of TiO₂ resulted in a band-gap narrowing, as the p states of N contribute to the narrowing by mixing with O 2p states. Cristiana et al. [83] have studied the defect states in reduced and n-type doped TiO₂ based on DFT + U and hybrid functionals (B3LYP). Both localized/delocalized solutions close in energy were found in the calculations, indicating that measurable temperature effects in determining the nature of

the defect states can be used in experiment. Theoretical studies of carbon doped TiO₂ (both rutile and anatase) have been conducted by Kamisaka et al. [84] and Cristiana et al. [85] as carbon can work as both the anion doping and cation doping. Both groups found that carbon impurities induce several localized occupied states contributing to the observed red shift of the absorption edge. Moreover, Cristiana et al. [85] also found that carbon doping might favor the formation of O vacancy in TiO₂. Co-doping with appropriate elements could significantly enhance the photocatalytic properties in TiO₂ owing to the existence of synergistic effects between doping elements, which can increase the visible light absorption and improve the separation efficiency of the electron-hole pairs [86–88]. For more detailed discussion about mono-doping and co-doping effects on the photocatalytic properties of TiO₂, we refer the reader to the review articles of Ref. [89–91]. Meng et al. [92] used Cu dopants to move the conduction band minimum (CBM) of α -Fe₂O₃ above the hydrogen redox level, while Ti dopants create very shallow donor levels and change the band-gap slightly. The above examples show that first-principles can be used to provide explanations of what is happening at the atomic level. However, first-principles should be able to provide guidelines for the search for new materials with improved band-gaps. The next example indicates what we can expect in the near future.

2.2. Charge Carrier Transport

Once the electron-hole pair is created, it needs to be separated; however, this is not a straight-forward process. The electron-hole pair feels a screened Coulomb attraction, and if it is strong enough, the electron-hole pair can be referred to as an exciton [93]. The attraction will affect the spatial distribution and transport properties of both the electron and the hole. However, as the wavefunction of the electron-hole pair becomes uncorrelated, the electron-hole pair can be viewed as free carriers. The charge carrier with the lowest effective mass (remember the second derivative of the dispersion relation) will exhibit a larger root-mean-square motion as compared to the heavier charge carrier. This implies that the lighter carrier will effectively create a charge separation, known as the photo-Dember effect [94]. This is the main effect that determines carrier transport under zero-field conditions.

However, this separation is rarely sufficient enough to be the main mechanism in photoelectrochemistry; instead, it is the presence of an interface that allows for an efficient separation of the electron-hole pairs. This is well-known from the semiconductor physics where interfaces, in the form of p-n junctions, are used to separate electron-hole pairs. Over the interface, a space charge layer is normally formed, owing to the difference in electrochemical potentials [95]. As the system equilibrates, i.e., electrons flow from higher potential to lower until the compensating field is sufficient to stop the flow, resulting in a parabolic bending of the semiconductor bands [95].

In a photoelectrochemical system, the interface is instead between the semiconductor and the liquid phase, see Figure 4. However, owing to the mobile charge carriers in the liquid, a Schottky junction is formed, which has a redistribution of the charge on the electrolyte side, effectively forming the Helmholtz layer. The field in the semiconductor can extend several of hundred Angstroms, depending on the doping level of the semiconductor. Conventional models all assume a uniform dopant distribution, and it remains unclear how the composition and atomic structure of the semiconductor affect the electronic structure, i.e., barrier height and band bending, on the atomic level. It should be noted, however, that recent advances [96–99] have made it possible to characterize the Schottky band bending at the nanometer scale and have revealed important deviations from predictions made on the conventional Schottky model [100]. Instead, the results, which depend on materials' properties, dopant compositions and concentrations, can be qualitatively interpreted in the inhomogeneous Schottky barrier height model [101–103]. Interestingly theory studies [104] show that the band bending is inhomogeneous and highly localized to the defect region, see Figure 5. This indicates a much more complicated band bending picture in real systems.

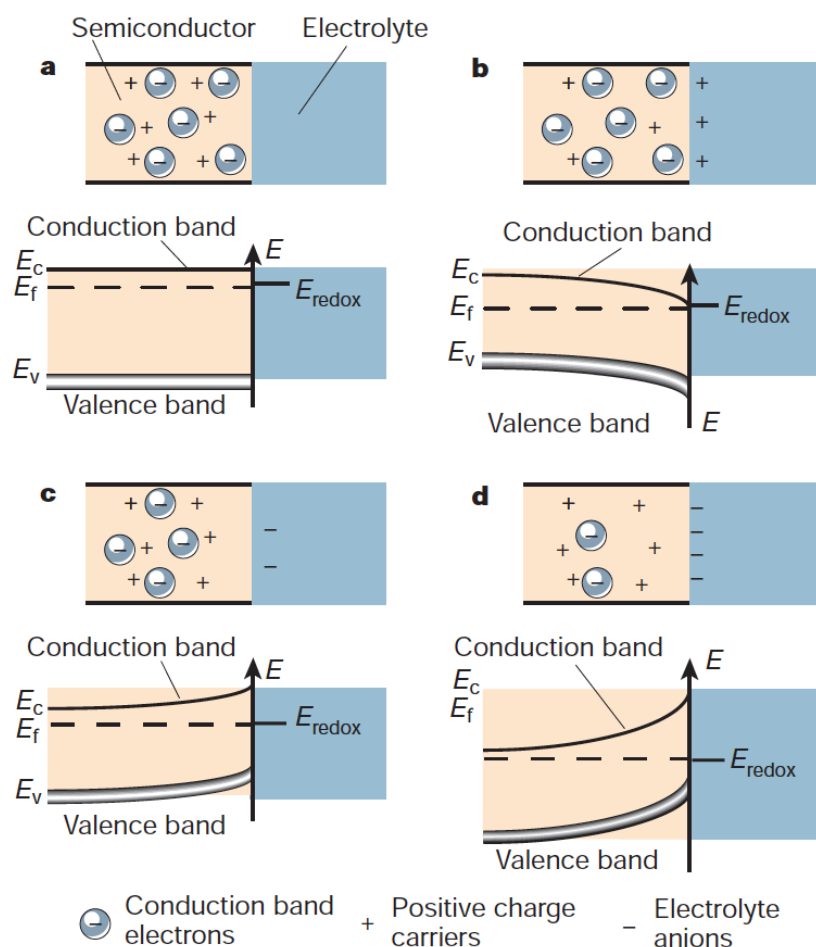


Figure 4. Schematic picture showing the electronic energy levels at the interface between an n-type semiconductor and an electrolyte containing a redox couple. The four cases indicated are: (a) flat band potential, where no space-charge layer exists in the semiconductor; (b) accumulation layer, where excess electrons have been injected into the solid producing a downward bending of the conduction and valence band towards the interface; (c) depletion layer, where electrons have moved from the semiconductor to the electrolyte, producing an upward bending of the bands; and (d) inversion layer, where the electrons have been depleted below their intrinsic level, enhancing the upward band bending and rendering the semiconductor p-type at the surface [96]. Reprinted by permission from Macmillan Publishers Ltd.: Nature 414 338, copyright 2001.

This field will assist in the separation of the photogenerated electron-hole pairs and drive the minority carrier to the surface, while picking up the excess energy from the field. This implies that the carriers can arrive at the surface with an excess energy corresponding the degree of bend banding, i.e., hot carriers. Note that in the space-charge layer, the carrier-carrier interaction is much less, and in principle only the phonon channel is open for the dissipation of energy. In contrast, the majority carrier will experience both the carrier-carrier and phonon-scattering processes during its propagation through the semiconductor material.

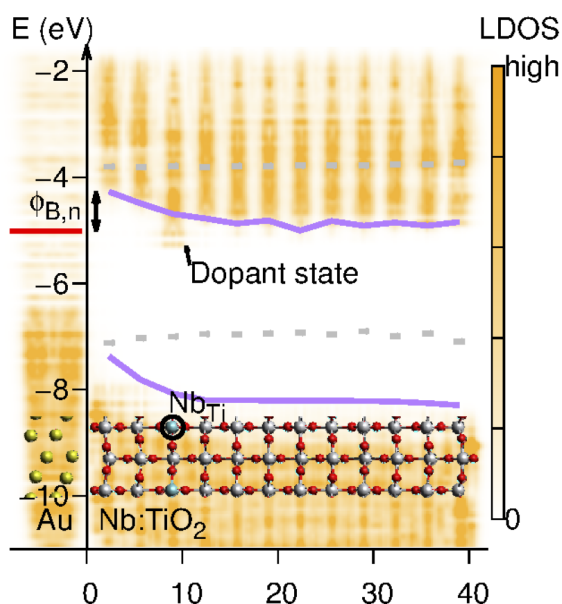


Figure 5. The color map shows the local density of states (LDOS) along the direction normal to the interface. The Nb-dopant is marked as Nb_{Ti} in the inserted structure plot. The dopant state below the bottom of the conduction band traps most of the excess electron donated by Nb_{Ti}. The band edges of the pristine TiO₂ are also shown (gray dashed lines). The band bending is caused by the dopant-induced charge polarization. Reprinted with permission from ref. [104].

As the electron or hole is transported through the lattice, the lattice responds to this charge by delocalizing it over many atoms (a large polaron) or by localizing it over just a few atoms (a small polaron). As the extra charge carrier will fill or empty states with the bonding or antibonding characteristics of the lattice atoms, the charge influences bond lengths and angles in the material. If the charge is delocalized, the influence is small because it is spread over many atoms, while a highly localized charge dramatically distorts the lattice. One way to view the process is to consider the carriers dragging a cloud of phonons along as it propagates through the lattice. This gives rise to an understanding of the phenomena of self-trapping. A small polaron will shift the surrounding lattice to its new position within a few lattice vibrations. This increases the stability of the state, creating a deeper potential well that must be overcome to transfer the polaron to a neighboring lattice site, i.e., there is a large reorganization energy associated with small polarons [105,106].

The excited charge carriers (electrons/holes) transport mainly through the hopping of small polarons in many metal oxides [105,107]. The description of the mobility of the small polarons are within the framework of the Marcus theory [108], of which the associated parameters can be calculated with quantum-mechanical calculation methods such as DFT, including DFT + U, hybrid functionals and Δ -self consistent field (Δ SCF) [109,110] to describe the localization of the trapped carriers [111–117].

Deskins et al. [118] studied the effect on adding one excess electron to the electronic structure of bare and singly hydroxylated rutile (110) surfaces. The excess electron formed a small polaron with its spin density and associated lattice distortion localized around a single site. Further, surface hydroxyl only perturbs the electronic potential slightly, and both clean and hydroxylated surfaces exhibit similar polaron stability. In the case of holes introduced into the electronic structure, the lattice distortions around hole polarons were found to be larger than around electron polarons [119], and holes were formed by removal of an O(2p) valence electron. Combining DFT and Marcus/Holstein theory of electron/polaron transfer (where reorganization energy and electronic coupling were taken into account) [120–122], the hole hopping was shown to be equal in all directions in rutile, whereas in anatase, one direction was found to be adiabatic in character, i.e., thermal processes coupled to phonons. Furthermore, the study [119] showed that holes are thermodynamically more stable in the

rutile phase, while electrons are more stable in the anatase phase. In a related study, Valentin et al. [123] showed that in order to describe localized defect states on reduced and hydroxylated $\text{TiO}_2(110)$, it is necessary to go beyond semi-local description of the exchange-correlation functional and use hybrid exchange functionals instead. Even though the electron trapping nature of $\text{Ti}(\text{OH})$ groups was verified through lattice distortion [124], no support that these defects also act as hole traps was found. On the other hand, the ΔSCF method [109,110] enable us the addition/substraction of the electron density of the specified orbital at each SCF cycle [117]. Within this scheme, Zawadzki et al. [111] has studied the electron/hole self-trapping in different anatase and rutile surface facets. Their results indicate that the position of the hole trapping states in the band-gap varies among rutile and anatase facets. Ji et al. [125] reported that the bridge oxygen is the most stable hole trapping site based on their DFT + U methods. First-principles studies on carrier transport in hematite showed that substitutional doping of Al benefits small polaron migration, thus resulting in an improvement in conductivity compared to the undoped sample [126]. Liao and Carter [127], on the other hand, investigated how the activation energies for hole diffusion were affected by different dopants. The study suggests that hole hopping was via oxygen anions for hematite and that hole carriers are predicted to be attracted to O anions near the dopants. Adelstein et al. [128] studied small polaron mobility in hematite with DFT + U methods. In their work, both the prefactor and activation energies for adiabatic polaron transport were calculated.

The examples above indicate that DFT is able to characterize carrier transport, in particular electron/hole polarons. However, there remains still some development before DFT can be to calculate all details involved in the electron-hole transport process. Especially the difficulty to have an adequate description of the energy difference between a localized and a delocalized state is crucial [129], and the predictive power of DFT is hampered by the need to compare with experiment. In a recent review Shluger et al. [130] give more examples of modeling of electron and hole trapping in metal oxides, and also the discussion concerning the different challenges involved.

The major challenge of the transport of photoexcited carriers in real material is the recombination of electrons and holes [25,36,131]. Crystal structure, crystallinity and particle size strongly affect the separation and migration of the photoexcited carriers. The defects normally work as the trapping sites and recombination centers which is harmful to the transport of electrons and holes. Therefore, highly crystalline and stoichiometric materials have fewer defects with a high photocatalytic activity. On the other hand, the diffusion distance of electrons or holes to surface active sites becomes shorter in nanosized materials which can decrease the recombination probability. Moreover, nanosized materials usually have high surface to volume ratio, which contributes to effective interaction between charge carriers and surface active sites [25].

In addition, the morphology of oxide thin films, defect structures, and the electrolyte composition [40,132–138] all can affect the transport of the photo-excited carriers. Nanostructured materials such as nanotubes with one dimensional structure can enhance the charge collection efficiency by providing direct transport pathway [132]. Moreover, in the dye-sensitized solar cell, larger surface area can improve the loading of dye molecules which can combine with the increased transport pathways in the nanotubes to improve the carrier collection and electron-hole separation [139,140]. In colloidal semiconductors, such as, TiO_2 and ZnO , semiconducting polymers, and amorphous organic photoconductors, the transport of the carriers can be described in terms of a multiple trapping model [141–143], which is determined by the chemical composition and microscopic structure of the material [133,136]. In this model, charge transport is treated as the transfer of carriers between localized states or traps, which originates from the defects states associated with oxygen vacancies in noncrystalline TiO_2 [136,137].

2.3. Electrochemical Surface Reactions

Once the hole arrives at the semiconductor-liquid interface, there is a clear analogy with the microscopic processes involved in an electrochemical cell. This is very beneficial as the recent

developments in computational electrochemistry have been quite remarkable. The frameworks put-forth by, e.g., the Anderson group [144–149], Neurock group [150–154], and the Rossmeisl/Norskov [155–162] group has provided a molecular-level insight into the atomic-scale processes that occur at the vicinity of the anode/cathode surface. As a natural extension, based on the electrochemical framework suggested by Rossmeisl/Norskov group, Valdes et al. [163–165] suggested a theoretical framework in which the photo-oxidation of water can be described by first-principles methods. Here, the driving force for the reaction originates from the photoinduced hole at the edge of the valence/conduction band. Hence, in the scale obtained by aligning the energy levels of oxide semiconductors with the redox level of the standard hydrogen electrode, a deep valence band edge energy level will result in a larger thermodynamic driving force in the case of oxidation reactions. Although the framework treats only the thermodynamics of the reaction mechanism, it provides a methodology for a detailed atomistic understanding of photoelectrochemical water-splitting.

The standard hydrogen electrode (SHE) plays a crucial role in the computational electrochemical framework [166], as the SHE is by definition zero when the chemical potential of the $\text{H}^+(\text{aq}) + \text{e}^-$ pair is equal to that of $1/2 \text{H}_2$ in the gas-phase. This circumvents the problem of calculating the energy of solvated protons and electrons and instead focuses on the gas-phase value of H_2 , which is easily described by first-principles. Entropy contributions from the liquid phase are approximated by reference to the equilibrium pressure in contact with liquid water at 298.15 K and 0.0317 bar where the free energy of gas phase water is equal to the free energy of liquid water. This permits the use of gas-phase water to calculate the binding energies and its transformation into liquid-phase water when adding the entropy correction [157,159,161]. The free energy change of the reaction step involving the formation of O_2 is set to the experimentally-obtained value of 4.92 eV per O_2 molecule. The free energy of the reaction intermediates is calculated via DFT by also including the zero-point energy (ZPE) and vibrational contributions. Normally, the entropy contribution is low as the photoelectrochemical conditions are not so high in temperature. Furthermore, the effect of the electrode potential on the adsorption energies is simple to include by adding a stabilization of $+eU$ when appropriate. In principle, the adsorption energy of reaction intermediates can depend on the electrode potential. However, first-principles studies [167] indicate that this effect is small, e.g., the adsorption energies of $^*\text{O}$, $^*\text{H}$, and $^*\text{OH}$ are only changed slightly when an electric field in the range of $-0.3 \text{ V}/\text{\AA}$ to $0.3 \text{ V}/\text{\AA}$ is used. Assuming a double layer thickness of 3 \AA , the range corresponds to a potential of -0.9 V and 0.9 V with respect to the zero potential. Therefore, the primary effect of the electrode potential is to change the (free) energy of the electrons.

At the photoanode/electrolyte interface, the solvent water molecules may play an important role [168–170], see Figure 6 for a schematic overview. Contributions from the liquid phase are normally approximated by including several of water layers in the simulation [140,171–173]; however, there also exist more advanced models, e.g., Refs. [174,175]. Ab initio MD (AIMD) has offered key insights into the vibrational motion of higher-frequency modes of water adsorbed to titania [176,177], however, it is difficult to determine lower-frequency translational modes accurately due to the high computational cost of the simulation [178]. Classical Molecular dynamics study of water in contact with TiO_2 surfaces has been performed by Ritwik et al. [179]. It was found that water OH bond lengths, H–O–H bond angles and dipole moments are not affected by the nature of the surface, whereas the orientation of the water molecules in the first and second monolayer is influenced strongly. The water network, with its many hydrogen bonds, will have a large effect on the stability of the reaction intermediates, especially the ones that can contribute with more hydrogen bonds [168]. First-principles results show that OH-containing reaction intermediates, such as, $^*\text{OH}$ and $^*\text{OOH}$, can be stabilized up to 0.6 eV on Pt (111), whereas those of H and O are affected to a lesser extent, ca. 0.1 eV [167].

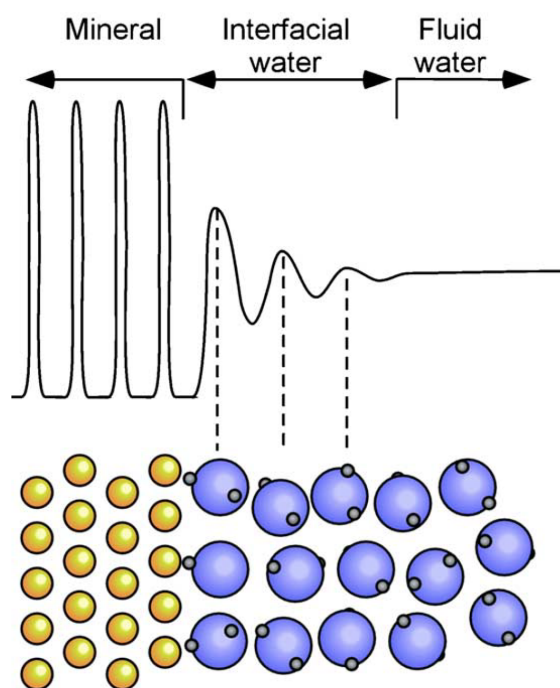


Figure 6. Schematic density profile of interfacial water near the solid–aqueous interface. Reprinted with permission from ref. [168]. Copyright 2004 Elsevier.

The main difference between the frameworks of electrochemistry and photoelectrochemistry is the origin of the driving potential [163,164]. In electrochemistry, this can be varied, whereas the photoelectrochemical driving force is the redox potential originating from the photoinduced hole in the valence band. Furthermore, it should be noted that the position of the valence band depends on the pH, however, the same dependence applies to the free energy of each reaction step for water oxidation [169]. Thus, to a first approximation, the thermodynamics of the photoelectrochemical reaction is unchanged by changes in the pH [180].

Pourbaix Surface Diagrams

The photoelectrochemical framework allows for the construction of the surface phase diagram, i.e., which reaction intermediates are adsorbed on the surface under specific pH and under dark or light conditions [181,182], e.g., see Figure 7. In electrochemistry, these phase diagrams are called Pourbaix diagrams [183–187] and is today a standard tool when investigating electrochemical reactions and include even novel techniques, such as machine learning [188]. Although Pourbaix diagrams were originally made for bulk transitions [189], the use of first-principles has shown that it can accurately describe which reaction intermediates are present and which are unstable under electrochemical conditions. The phase diagrams are only applied under stable conditions, which implies that the rate of holes that reach the surface needs to be greater than the back-reaction of water-splitting in order to build up a potential across the photoanode. Furthermore, it should be noted that the potential experienced by a metal nanoparticle at the surface of a photoelectrode during illumination is different from the externally-applied potential, as the quasi-Fermi level of holes shifts to positive potentials, leading to a shift in the Fermi level of the metal particle [169].

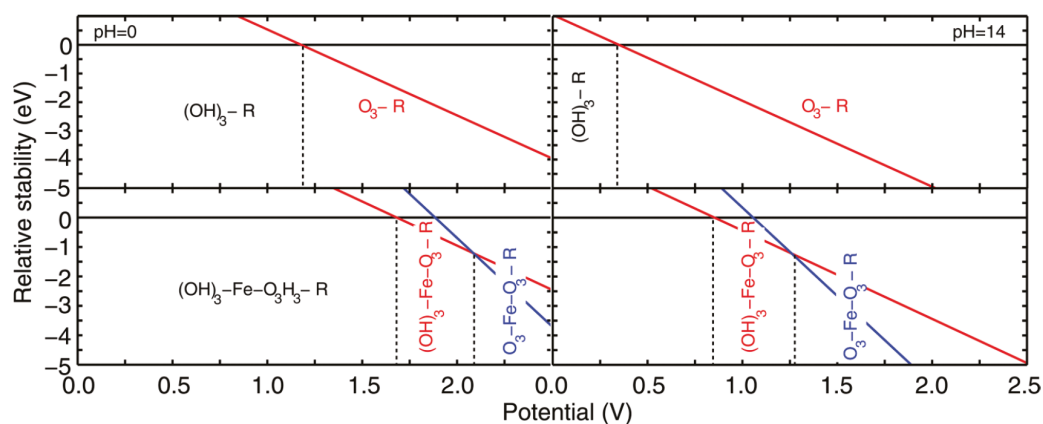


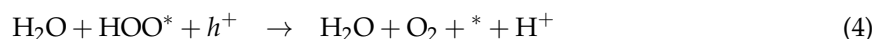
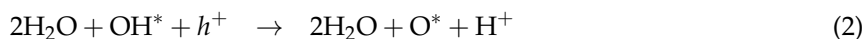
Figure 7. The relative stability of all considered surface terminations as a function of applied potential and at two different pH, namely pH = 0 (left) and pH = 14 (right). Reprinted with permission from [181]. Copyright 2011 American Chemical Society.

2.4. Reaction Mechanism

Although the overall water splitting reaction always evolves oxygen at the anode, the reaction mechanism depends on the pH of the electrolyte. Under acidic conditions, the water oxidation reaction is



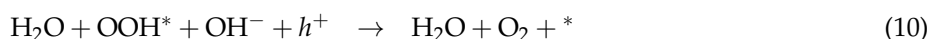
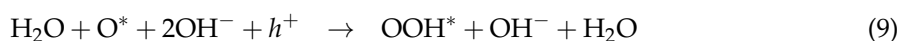
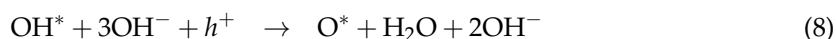
where the following simple reaction mechanism has been suggested in the literature [127,159,161,163,164,181,182,190], see Figure 8 for more details:



Under alkaline conditions, the water oxidation reaction is instead:



and analogously, the reaction mechanism can be written as:



In the theoretical electrochemical framework described above, the same reaction intermediates are present independently of the actual pH of the electrolyte. Direct recombination of oxygen atoms to O_2 was not considered, as this process is expected to be associated with a large barrier on metals and oxides [191].

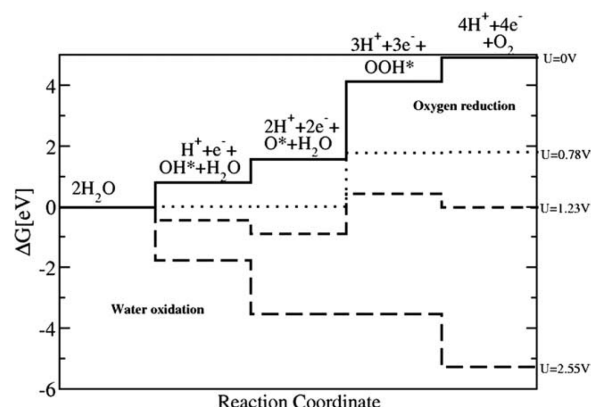


Figure 8. The water splitting reaction at different potentials. At potentials between 0 and 0.78 V all steps in the oxygen reduction are exothermic. For potentials beyond 2.55 V all water splitting reaction steps become exothermic. This variation is obtained by varying the term eU in the free energy per electron transferred to the electrode. Reprinted from Chemical Physics 319 (2005) 178, Copyright 2005, with permission from Elsevier [158].

The described photoelectrochemical framework has been used to study photo-induced water-oxidation on rutile $\text{TiO}_2(110)$ [163], WO_3 (various facets) [164], and $\text{Fe}_2\text{O}_3(0001)$ [181,182,190,192,193]. So far, the redox potential from the band edge of the valence band has been sufficient to make the reaction thermodynamically favorable. Only in the case of Fe_2O_3 was the water oxidation prohibited on some surface terminations, however these terminations were not the most stable ones, which implies that during normal operation conditions, these do not play a part [181].

The electrochemical framework that has been described so far does not easily lend itself to the calculation of activation barriers; hence, the kinetics of any reaction are still missing. There exist extensions that deal with this issue. For instance, by varying the number of protons/electrons in the electrolyte, Skulasson et al. [171,194] could determine the activation energy for the hydrogen evolution reaction as a function of electrode potential. Another approach focuses on charge transfer reactions that use a single barrier calculation in an electrochemical environment and use the knowledge of the surface charge at the initial, transition and final states to estimate the barrier [195].

2.5. Overpotential

Abild-Pedersen et al. [196] showed the existence of approximately linear relationships between the adsorption energy of hydrogen and non-hydrogen containing species, e.g., OH and O, over many different materials. In combination with Brønsted–Evans–Polanyi relations [197] this has allowed for fast computational screening of heterogeneous catalysts [198]. In electrochemistry, the same linear relations have been used to show that in the oxygen evolution reaction (OER) and the oxygen reduction reaction (ORR), there exists a fundamental overpotential [157,199–202]. This was done by calculating the difference in Gibbs free energy for each reaction step and, by use of the linear scaling relations, expressing each reaction intermediate as a function of one of these differences or a linear combination [199,200]. In Figure 9, the OER volcano plots over different substrates are shown. Furthermore, the fundamental overpotential, which originates from the fixed distance between the binding of OH and OOH, is also shown. This observation provides an upper limit on how good an OER electrocatalysts can be expected to be.

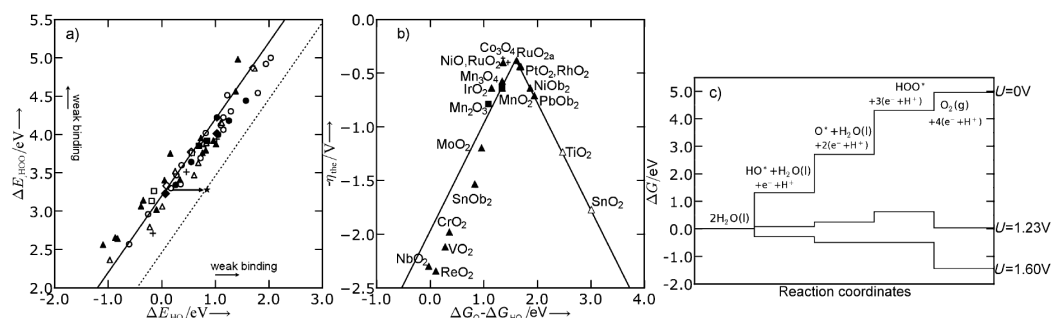


Figure 9. (a) Adsorption energies of HOO^* as a function of adsorption energies of HO^* on rutile, perovskites, anatase, Mn_xO_y , Co_3O_4 and NiO oxides. Open and solid symbols represent the adsorption energies on clean surfaces and on high-coverage surfaces, respectively. The star represents the binding energies required for an ideal electrocatalyst. The dotted line represents the relationship between ΔE_{HOO^*} and ΔE_{HO^*} for an ideal catalyst, which is given by $\Delta E_{\text{HOO}^*} = \Delta E_{\text{HO}^*} + 2.44 \text{ eV}$; (b) Activity trends toward oxygen evolution for rutile oxides, Co_3O_4 , and Mn_xO_y . The negative value of the theoretical overpotential is plotted as a function of the standard free energy of ΔG_{O^*} and ΔG_{OH^*} ; (c) Standard free-energy diagram for the OER on O^* -covered RuO_2 at three different potentials: $U = 0$, 1.23, and 1.60 V. Reprinted with permission from [200].

The origin of the fundamental overpotential provides directions of how to overcome this limitation. If a catalyst is able to stabilize $^*\text{OOH}$ with respect to $^*\text{OH}$ (i.e., make the free energy difference between $^*\text{OOH}$ and $^*\text{OH}$ to values closer to 2.46 eV), it will circumvent the fundamental overpotential. One suggested pathway would be to use 3D structures, which are able to differentiate between the intermediates e.g., by confining the OOH group. Hangman porphyrins have been suggested as possible candidates, which indeed have been shown to be good catalysts for OER [203–207]; however, there is no support of this claim from first-principles as of yet [208], see Figure 10.

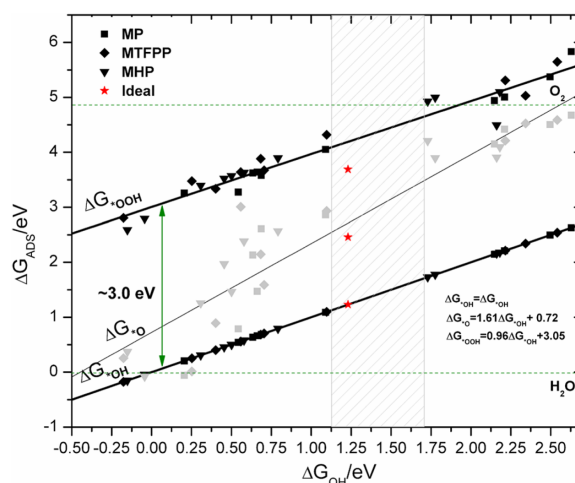


Figure 10. Scaling relation between the Gibbs free energies of adsorption of $^*\text{OH}$, $^*\text{O}$, and $^*\text{OOH}$. Squares represent metal porphyrine, triangles hangman metalloporphyrins and rectangles metaltetrafluorophenylporphyrins molecules, respectively. The dashed lines at 0 and 4.92 eV represent energy of H_2O and O_2 , respectively. The grey area separates the metals from the Group 9 and before from the 10 and after of the periodic table. Reprinted with permission from [208]. Copyright 2014 American Chemical Society.

It is interesting to note that the processes in the biological respiratory system [209] utilize a secondary coordination sphere around the active site, which allows for non-covalent interactions

with the reaction intermediates. In fact, the secondary coordination sphere appears to be a necessity in order to overcome energy barriers arising from the triplet ground state of the oxygen [210]. Designing a catalyst material that can mimic the interaction of the secondary coordination sphere remains a challenge, while potentially fruitful if successful.

3. Conclusions

Photoelectrochemistry is a very interesting topic covering various fields in chemistry and physics. Here, we have covered a selection of the many processes involved and discussed how first-principles methods can help in the interpretation and future improvements. The many success stories reveal a promising future, i.e., first-principles calculations will not be used solely to reproduce experimentally-known facts, but will become the standard starting point when a new photoelectrocatalyst for a known reaction is desired, or even when an unknown reaction to obtain a given product is needed.

However, there remain some issues that should be addressed and solved before this promise can come true. The use of more accurate exchange-correlation functionals seems to be able to push first-principles from being explanatory to predictive. This development will most certainly continue, and hopefully, band-gap design will soon be a reality. The problem associated with charge carrier transfer and the connection between DFT calculations of photoelectrocatalysis and dynamical simulations of electron transfer has not yet fully matured, although there exists a number of interesting developments. The use of the standard hydrogen electrode as the reference point has opened up the possibility to use first-principles methods with some easy to electrochemical and photoelectrochemical systems, at least when the information of the thermodynamics is key. The framework around kinetics is still being developed, but even in the light of these remaining issues, the future looks bright for first-principles and its impact on photoelectrochemistry.

Acknowledgments: The authors want to acknowledge the financial support of the Swedish research council, Formas, and the Chalmers Area of Advance Material Science and Area of Advance Energy are acknowledged.

Conflicts of Interest: The author declares no conflict of interest.

Appendix A. Theoretical Methodologies of Density Functional Theory [211,212]

Appendix A.1. The Hohenberg-Kohn Theorems

The central theorems of DFT are based on the theorems given by Hohenberg and Kohn (HK) [43]:

Theorem A1. *For any system of interacting particles in an external potential $V_{\text{ext}}(\mathbf{r})$, there is a one-to-one correspondence between the potentials and the ground-state particle density $n_0(\mathbf{r})$. The ground-state expectation value of any observable is a unique functional of the ground-state particle density $n_0(\mathbf{r})$:*

$$\langle \Psi | A | \Psi \rangle = A[n_0(\mathbf{r})]. \quad (\text{A1})$$

Theorem A2. *For any external potential applied to an interacting particle system, it is possible to define a universal total energy functional $E[n(\mathbf{r})]$ of the particle density $n(\mathbf{r})$, written as*

$$E[n(\mathbf{r})] = F_{\text{HK}}[n(\mathbf{r})] + \int d\mathbf{r} V_{\text{ext}}(\mathbf{r}) n(\mathbf{r}), \quad (\text{A2})$$

where $F_{\text{HK}}[n(\mathbf{r})]$ includes all the electron-electron interaction and the kinetic energy of the interacting particle system. The global minimum of this functional is the exact ground-state total energy of the system, E_0 , and the particle density that minimizes this functional is the exact ground-state density $n_0(\mathbf{r})$. The first theorem implies that all ground-state properties of a system can be completely obtained by only the ground-state density. It emphasizes the importance of the ground-state density. The second theorem indicates that the ground-state

density can be determined by the minimization of the energy functional, which can further be used to compute other ground-state observables.

Appendix A.2. The Kohn-Sham Equations

The Kohn and Sham ansatz [213] states that the interacting many-body problem can be replaced by a corresponding one-particle non-interacting system, where the total energy functional can be written as

$$E[n(\mathbf{r})] = T_0[n(\mathbf{r})] + \int V_{ext}n(\mathbf{r})d\mathbf{r} + \frac{1}{2} \int \int \frac{n(\mathbf{r})n(\mathbf{r}')}{|\mathbf{r} - \mathbf{r}'|} d\mathbf{r}' d\mathbf{r} + E_{xc}[n(\mathbf{r})] + E_{II}, \quad (\text{A3})$$

which is the so-called Kohn-Sham functional. The first and second terms in Equation (A3) are the functional of the kinetic energy, and the external potential describing the interaction between nuclei and valence electrons. The third term is the Coulomb potential (Hartree term), and the fourth term is the exchange-correlation functional, which includes all many-body effects of exchange and correlation, but also the missing contribution to the kinetic energy of interacting electrons. This is the only term that cannot be evaluated exactly, and should be described by different approximations. The last term is the energy contribution from the interaction of nuclei. Using the variational principle to minimize the Kohn-Sham functional with respect to the density $n(\mathbf{r})$ leads to the one-particle Kohn-Sham equations

$$\left(\frac{-\hbar^2}{2m_e} \nabla^2 + V_{KS} \right) \varphi_i(\mathbf{r}) = \varepsilon_i \varphi_i(\mathbf{r}) \quad (\text{A4})$$

where ε_i are the eigenvalues, $\varphi_i(\mathbf{r})$ are the K-S orbitals and V_{KS} is the K-S potential,

$$V_{KS} = V_{ext} + \int \frac{n(\mathbf{r}')}{|\mathbf{r} - \mathbf{r}'|} d\mathbf{r}' + V_{xc}, \quad (\text{A5})$$

with the exchange-correlation potential defined by

$$V_{xc} = \frac{\delta E_{xc}[n]}{\delta n(\mathbf{r})}. \quad (\text{A6})$$

One thing that we should bear in mind is that the Kohn-Sham equations describe non-interacting electrons. The Kohn-Sham orbitals, $\varphi_i(\mathbf{r})$, have no physical meaning. But the density obtained from the Kohn-Sham equation and the density of the system of interacting electrons should be the same. If the exchange-correlation potential is defined, the ground state density and energy can be obtained by solving the single-particle Kohn-Sham equations. However, the effective potential depends on the electron density, which depends on the Kohn-Sham orbitals, which, in turn, depends on the effective potential, therefore, one needs to solve the Kohn-Sham equations in a self-consistent manner.

Appendix A.3. The Exchange and Correlation Functionals

The main challenge for practical use of the Kohn-Sham equations is to find a good approximation for the exchange-correlation functional. Numerous approximations have been proposed. Most commonly used exchange-correlation functionals will be briefly discussed in the following part.

In the local-density approximation (LDA) approximation, the exchange-correlation functional energy is evaluated from the exchange-correlation energy for the homogeneous electron gas [214]. The E_{xc} as a function of density within each volume can be assumed as the one derived from the

uniform electron gas for that density. The total exchange-correlation energy of the system can be written as

$$E_{xc}^{LDA}[n(\mathbf{r})] = \int d\mathbf{r} n(\mathbf{r}) \epsilon_{XC}^{hom}[n(\mathbf{r})] \quad (A7)$$

where $\epsilon_{XC}^{hom}[n(\mathbf{r})]$ is the exchange-correlation energy density of a homogenous gas with density $n(\mathbf{r})$. In practice, the exchange and correlation energy of the homogeneous electron gas can be calculated separately. The form of the exchange energy is well-known with a simple analytical expression [212] and the correlation energy has been calculated accurately with quantum Monte Carlo method [215].

In principle, LDA can only be valid for systems with slowly varying densities. Calculations performed with this method for atoms, molecules and solids show that Equation (A7) also works surprisingly well for these systems. However, LDA indeed has some accuracy problems. For example, it tends to overestimate cohesive energies and underestimate the lattice constants for metals and insulators [216,217].

One way to improve LDA is to include the gradient of the density $\nabla n(\mathbf{r})$ instead of only including the local density $n(\mathbf{r})$. This is the so-called generalized gradient approximation (GGA) [218–220]. Such a functional can be described as

$$E_{xc}^{GGA}[n(\mathbf{r})] = \int d\mathbf{r} n(\mathbf{r}) \epsilon_{XC}(n(\mathbf{r}), |\nabla n(\mathbf{r})|) = \int d\mathbf{r} n(\mathbf{r}) \epsilon_X^{hom} F_{XC}(n(\mathbf{r}), |\nabla n(\mathbf{r})|), \quad (A8)$$

where E_{XC} is a functional of the density $n(\mathbf{r})$ and the gradient of the density $\nabla n(\mathbf{r})$ and the ϵ_X^{hom} is the exchange energy of a homogeneous electron gas. The GGA-functionals have many parameterizations for example, such as B88 by Becke [221], PW91 by Perdew and Wang [222] and PBE by Perdew, Burke and Ernzerhof [223]. With the inclusion of the gradient of the density $\nabla n(\mathbf{r})$, GGA can result in better agreement with experiment than LDA for many properties of molecule and solids such as geometries and ground state energies.

Recently, the functional for “GGAs for solids” (e.g., AM05 [224] and PBEsol [60]) have been proposed. They produce rather accurate lattice constants and surface energies, but give poor atomization energies.

The meta-GGAs are the third generation functionals, which includes the second derivative of the density, $\nabla^2 n(\mathbf{r})$, and/or the kinetic energy density, τ_σ , in the exchange and correlation potential. Functionals of this type are, for example, TPSS [225], revTPSS [226] and AM06-L [227]. The meta-GGAs improve the accuracy of results further and predicting good agreement with experiment for lattice constants, surface energies as well as atomization energies.

A mixing scheme of some exact exchange with the exchange and correlation from DFT is employed in hybrid functionals. Becke proposed an adiabatic connection formula which can be used as a starting point for a hybrid functional [228].

$$E_{XC} = \int_0^1 d\lambda E_{XC}^\lambda, \quad (A9)$$

where E_{XC} is the exchange-correlation energy and λ scales the contribution from exact exchange. This formula is the connection between the non-interacting system and the fully interacting one with density $n(\mathbf{r})$. In the $\lambda = 0$ limit, it restores to the Kohn-Sham non-interacting particles system. B3LYP (Becke, three-parameter, Lee-Yang-Parr) [229–231] is most widely used especially in quantum chemistry, where three parameters (determined by fitting to experiment) are employed to treat the mixing of exact exchange and the DFT exchange-correlation. The Heyd-Scuseria-Ernzerhof (HSE) hybrid functional is a hybrid density functional based on a screened Coulomb potential for the exchange interaction [69]. Using a screened Coulomb potential for Hartree-Fock (HF) exchange enables fast and accurate hybrid calculations, where the Coulomb potential are decomposed into a long-range

and a short range part. In practice, the splitting of the full Coulomb potential is done by means of error functions

$$E_{XC}^{\omega PBEh} = aE_X^{HF,SR}(\omega) + (1-a)E_X^{PBE,SR}(\omega) + E_X^{PBE,LR}(\omega) + E_C^{PBE}, \quad (A10)$$

where a is the mixing parameter and ω is the adjustable parameter controlling the short-range of interactions beyond which the short range interactions becomes negligible. HSE06 with standard value of $a = 0.25$ and $\omega = 0.2$ have been shown to yield good results for many systems. The PBE0 functional [70] can be obtained for $\omega = 0$. $E_X^{HF,SR}(\omega)$ is the short range exact exchange energy. $E_X^{PBE,SR}(\omega)$ and $E_X^{PBE,LR}(\omega)$ are the short and long range components of the PBE exchange energy, respectively, and E_C^{PBE} is the PBE correlation energy. The M06 suite of functionals [227] contain a set of four meta hybrid GGA functionals, i.e., M06-L, M06, M06-2X and M06-HF, each of which has different amount of exact exchange. The M06-L is completely local without any HF exchange, and M06, M06-2X, and M06-HF have 27%, 54%, and 100% of HF exchange, respectively. The M06 suite mainly improves one of the big deficiencies of DFT in describing the dispersion forces. Each of them has the advantages to specific systems, for example, M06-HF is suitable for TD-DFT calculations of Rydberg and charge-transfer states.

References

- Verne, J. *L'Île Mystérieuse*; Pierre-Jules Hetzel: Chartres, France, 1874.
- Campbell, C.J.; Laherrère, J.H. The End of Cheap Oil. *Sci. Am.* **1998**, *278*, 60–65.
- Bentley, R.; Boyle, G. Global Oil Production: Forecasts and Methodologies. *Environ. Plan. B Plan. Des.* **2008**, *35*, 609–626.
- Hook, M.; Tang, X. Depletion of fossil fuels and anthropogenic climate change—A review. *Energy Policy* **2013**, *52*, 797–809.
- BP Statistical Review of World Energy. 2016. Available online: <http://www.bp.com/en/global/corporate/energy-economics/statistical-review-of-world-energy.html> (accessed on 5 March 2017).
- Gerland, P.; Raftery, A.; Ševčíková, H.; Li, N.; Gu, D.; Spoorenberg, T.; Alkema, L.; Fosdick, B.; Chunn, J.; Lalic, N.; et al. World population stabilization unlikely this century. *Science* **2014**, *346*, 234–237.
- Jones, G.A.; Warner, K.J. The 21st century population-energy-climate nexus. *Energy Policy* **2016**, *93*, 206–212.
- Smalley, R.E. Future Global Energy Prosperity: The Terawatt Challenge. *MRS Bull.* **2005**, *30*, 412–417.
- Lewis, N.S. Toward Cost-Effective Solar Energy Use. *Science* **2007**, *315*, 798–801.
- Armaroli, N.; Balzani, V. The Future of Energy Supply: Challenges and Opportunities. *Angew. Chem. Int. Ed.* **2007**, *46*, 52–66.
- Vesborg, P.C.K.; Jaramillo, T.F. Addressing the terawatt challenge: Scalability in the supply of chemical elements for renewable energy. *RCS Adv.* **2012**, *2*, 7933–7947.
- Seh, Z.W.; Kibsgaard, J.; Dickens, C.F.; Chorkendorff, I.; Nørskov, J.K.; Jaramillo, T.F. Combining theory and experiment in electrocatalysis: Insights into materials design. *Science* **2017**, *355*, eaad4998.
- Rajeshwar, K.; McConnell, R.; Harrison, K.; Licht, S. *Solar Hydrogen Generation—Toward a Renewable Energy Future*; Springer: Berlin, Germany, 2008.
- Herron, J.A.; Kim, J.; Upadhye, A.A.; Huber, G.W.; Maravelias, C.T. A general framework for the assessment of solar fuel technologies. *Energy Environ. Sci.* **2015**, *8*, 1754–5692.
- Acar, C.; Dincer, I.; Naterer, G.F. Review of photocatalytic water-splitting methods for sustainable hydrogen production. *Int. J. Energy Res.* **2016**, *40*, 1449–1473.
- Junge, H.; Rockstroh, N.; Fischer, S.; Brückner, A.; Ludwig, R.; Lochbrunner, S.; Kühn, O.; Beller, M. Light to Hydrogen: Photocatalytic Hydrogen Generation from Water with Molecularly-Defined Iron Complexes. *Inorganics* **2017**, *5*, 14.
- Dura, L.; Wächtler, M.; Kupfer, S.; Kübel, J.; Ahrens, J.; Höfler, S.; Bröring, M.; Dietzek, B.; Beweries, T. Photophysics of BODIPY Dyes as Readily-Designable Photosensitisers in Light-Driven Proton Reduction. *Inorganics* **2017**, *5*, 21.
- Li, C.T.; Lin, R.Y.Y.; Lin, J.T. Sensitizers for Aqueous-Based Solar Cells. *Chem. Asian J.* **2017**, *12*, 486–496.

19. Kakiage, K.; Aoyama, Y.; Yano, T.; Oya, K.; Fujisawa, J.i.; Hanaya, M. Highly-efficient dye-sensitized solar cells with collaborative sensitization by silyl-anchor and carboxy-anchor dyes. *Chem. Commun.* **2015**, *51*, 15894–15897.
20. Galliano, S.; Bella, F.; Gerbaldi, C.; Falco, M.; Viscardi, G.; Grätzel, M.; Barolo, C. Photoanode/Electrolyte Interface Stability in Aqueous Dye-Sensitized Solar Cells. *Energy Technol.* **2017**, *5*, 300–311.
21. Bella, F.; Galliano, S.; Falco, M.; Viscardi, G.; Barolo, C.; Gratzel, M.; Gerbaldi, C. Approaching truly sustainable solar cells by the use of water and cellulose derivatives. *Green Chem.* **2017**, *19*, 1043–1051.
22. Bella, F.; Galliano, S.; Falco, M.; Viscardi, G.; Barolo, C.; Gratzel, M.; Gerbaldi, C. Unveiling iodine-based electrolytes chemistry in aqueous dye-sensitized solar cells. *Chem. Sci.* **2016**, *7*, 4880–4890.
23. Walter, M.G.; Warren, E.L.; McKone, J.R.; Boettcher, S.W.; Mi, Q.; Santori, E.A.; Lewis, N.S. Solar Water Splitting Cells. *Chem. Rev.* **2010**, *110*, 6446–6473.
24. Pinaud, B.A.; Benck, J.D.; Seitz, L.C.; Forman, A.J.; Chen, Z.; Deutsch, T.G.; James, B.D.; Baum, K.N.; Baum, G.N.; Ardo, S.; et al. Technical and economic feasibility of centralized facilities for solar hydrogen production via photocatalysis and photoelectrochemistry. *Energy Environ. Sci.* **2013**, *6*, 1983–2002.
25. Jafari, T.; Moharreri, E.; Amin, A.S.; Miao, R.; Song, W.; Suib, S.L. Photocatalytic Water Splitting—The Untamed Dream: A Review of Recent Advances. *Molecules* **2016**, *21*, 900.
26. Navarro Yerga, R.; Álvarez Galván, M.; del Valle, F.; Villoria de la Mano, J.; Fierro, J. Water Splitting on Semiconductor Catalysts under Visible-Light Irradiation. *ChemSusChem* **2009**, *2*, 471–485.
27. Xing, J.; Fang, W.Q.; Zhao, H.J.; Yang, H.G. Inorganic Photocatalysts for Overall Water Splitting. *Chem. Asian J.* **2012**, *7*, 642–657.
28. Osterloh, F.E. Inorganic nanostructures for photoelectrochemical and photocatalytic water splitting. *Chem. Soc. Rev.* **2013**, *42*, 2294–2320.
29. Ran, J.; Zhang, J.; Yu, J.; Jaroniec, M.; Qiao, S.Z. Earth-abundant cocatalysts for semiconductor-based photocatalytic water splitting. *Chem. Soc. Rev.* **2014**, *43*, 7787–7812.
30. Hisatomi, T.; Kubota, J.; Domen, K. Recent advances in semiconductors for photocatalytic and photoelectrochemical water splitting. *Chem. Soc. Rev.* **2014**, *43*, 7520–7535.
31. Fujishima, A.; Honda, K. Electrochemical Photolysis of Water at a Semiconductor Electrode. *Nature* **1972**, *238*, 37.
32. Rajeshwar, K. Fundamentals of Semiconductor Electrochemistry and Photoelectrochemistry. In *Encyclopedia of Electrochemistry*; Wiley-VCH: Berlin, Germany, 2007.
33. Van de Krol, R.; Grätzel, M. *Photoelectrochemical Hydrogen Production*; Springer: Berlin, Germany, 2012.
34. Lewerenz, H.J.; Peter, L. *Photoelectrochemical Water Splitting: Materials, Processes and Architectures*; Royal Society of Chemistry: Cambridge, UK, 2013.
35. Ni, M.; Leung, M.K.; Leung, D.Y.; Sumathy, K. A review and recent developments in photocatalytic water-splitting using for hydrogen production. *Renew. Sustain. Energy Rev.* **2007**, *11*, 401–425.
36. Kudo, A.; Miseki, Y. Heterogeneous photocatalyst materials for water splitting. *Chem. Soc. Rev.* **2009**, *38*, 253–278.
37. Dau, H.; Limberg, C.; Reier, T.; Risch, M.; Roggan, S.; Strasser, P. The Mechanism of Water Oxidation: From Electrolysis via Homogeneous to Biological Catalysis. *ChemCatChem* **2010**, *2*, 724–761.
38. Zhang, X.; Bieberle-Hütter, A. Modeling and Simulations in Photoelectrochemical Water Oxidation: From Single Level to Multiscale Modeling. *ChemSusChem* **2016**, *9*, 1223–1242.
39. Roger, I.; Shipman, M.A.; Symes, M.D. Earth-abundant catalysts for electrochemical and photoelectrochemical water splitting. *Nat. Rev. Chem.* **2017**, *1*, 3.
40. Iandolo, B.; Wickman, B.; Zoric, I.; Hellman, A. The rise of hematite: Origin and strategies to reduce the high onset potential for the oxygen evolution reaction. *J. Mater. Chem. A* **2015**, *3*, 16896–16912.
41. Montoya, J.H.; Seitz, L.C.; Chakthranont, P.; Vojvodic, A.; Jaramillo, T.F.; Norskov, J.K. Materials for solar fuels and chemicals. *Nat. Mater.* **2017**, *16*, 70–81.
42. Bak, T.; Nowotny, J.; Rekas, M.; Sorrell, C. Photo-electrochemical hydrogen generation from water using solar energy. Materials-related aspects. *Int. J. Hydrog. Energy* **2002**, *27*, 991–1022.
43. Hohenberg, P.; Kohn, W. Inhomogeneous Electron Gas. *Phys. Rev.* **1964**, *136*, B864–B871.
44. Jones, R.O. Density functional theory: Its origins, rise to prominence, and future. *Rev. Mod. Phys.* **2015**, *87*, 897–923.

45. Hasnip, P.J.; Refson, K.; Probert, M.I.J.; Yates, J.R.; Clark, S.J.; Pickard, C.J. Density functional theory in the solid state. *Philos. Trans. R. Soc. Lond. A Math. Phys. Eng. Sci.* **2014**, *372*, 20130270.
46. Parr, R.G.; Yang, W. *Density-Functional Theory of Atoms and Molecules*; Oxford University Press: New York, NY, USA, 1989.
47. Dreizler, R.M.; Gross, E.K.U. *Density-Functional Theory: An Approach to the Quantum Many-Body Problem*; Springer: Berlin, Germany, 1990.
48. Fiolhais, C.; Nogueira, F.; Marques, M. *A Primer in Density Functional Theory*; Springer: Berlin/Heidelberg, Germany, 2003.
49. Curtarolo, S.; Hart, G.L.W.; Nardelli, M.B.; Mingo, N.; Sanvito, S.; Levy, O. The high-throughput highway to computational materials design. *Nat. Mater.* **2013**, *12*, 191–201.
50. Jain, A.; Shin, Y.; Persson, K.A. Machine learning bandgaps of double perovskites. *Nat. Rev. Mater.* **2016**, *1*, 15004.
51. Dai, H.L.; Ho, W. *Spectroscopy and Photochemistry on Metal Surfaces*; World Scientific: Singapore, Singapore, 1995.
52. Liebsch, A. *Electronic Excitations at Metal Surfaces*; Plenum Press: Berlin, Germany, 1997.
53. Nozik, A.J. Spectroscopy and hot electron relaxation dynamics in semiconductor quantum wells and quantum dots. *Annu. Rev. Phys. Chem.* **2001**, *52*, 193–231.
54. Brongersma, M.L.; Halas, N.J.; Nordlander, P. Plasmon-induced hot carrier science and technology. *Nat. Nano* **2015**, *10*, 25–34.
55. Saavedra, J.R.M.; Asenjo-Garcia, A.; García de Abajo, F.J. Hot-Electron Dynamics and Thermalization in Small Metallic Nanoparticles. *ACS Photonics* **2016**, *3*, 1637–1646.
56. Ogawa, T.; Yanai, N.; Monguzzi, A.; Kimizuka, N. Highly Efficient Photon Upconversion in Self-Assembled Light-Harvesting Molecular Systems. *Sci. Rep.* **2015**, *5*, 10882.
57. Godby, R.W.; Schlüter, M.; Sham, L.J. Trends in self-energy operators and their corresponding exchange-correlation potentials. *Phys. Rev. B* **1987**, *36*, 6497–6500.
58. Godby, R.W.; Schlüter, M.; Sham, L.J. Self-energy operators and exchange-correlation potentials in semiconductors. *Phys. Rev. B* **1988**, *37*, 10159–10175.
59. Hafner, J. Ab-initio simulations of materials using VASP: Density-functional theory and beyond. *J. Comput. Chem.* **2008**, *29*, 2044–2078.
60. Perdew, J.P.; Ruzsinszky, A.; Csonka, G.I.; Vydrov, O.A.; Scuseria, G.E.; Constantin, L.A.; Zhou, X.; Burke, K. Restoring the Density-Gradient Expansion for Exchange in Solids and Surfaces. *Phys. Rev. Lett.* **2008**, *100*, 136406.
61. Kuisma, M.; Ojanen, J.; Enkovaara, J.; Rantala, T.T. Kohn-Sham potential with discontinuity for band gap materials. *Phys. Rev. B* **2010**, *82*, 115106.
62. Hedin, L. New Method for Calculating the One-Particle Green's Function with Application to the Electron-Gas Problem. *Phys. Rev.* **1965**, *139*, A796–A823.
63. Castelli, I.E.; Hüser, F.; Pandey, M.; Li, H.; Thygesen, K.S.; Seger, B.; Jain, A.; Persson, K.A.; Ceder, G.; Jacobsen, K.W. New Light-Harvesting Materials Using Accurate and Efficient Bandgap Calculations. *Adv. Energy Mater.* **2015**, *5*, 1400915.
64. Pilania, G.; Mannodi-Kanakkithodi, A.; Uberuaga, B.P.; Ramprasad, R.; Gubernatis, J.E.; Lookman, T. Machine learning bandgaps of double perovskites. *Sci. Rep.* **2016**, *6*, 19375.
65. Gallino, F.; Pacchioni, G.; Valentin, C.D. Transition levels of defect centers in ZnO by hybrid functionals and localized basis set approach. *J. Chem. Phys.* **2010**, *133*, 144512, doi:10.1063/1.3491271.
66. Lany, S.; Zunger, A. Assessment of correction methods for the band-gap problem and for finite-size effects in supercell defect calculations: Case studies for ZnO and GaAs. *Phys. Rev. B* **2008**, *78*, 235104.
67. De Walle, C.G.V.; Neugebauer, J. First-principles calculations for defects and impurities: Applications to III-nitrides. *J. Appl. Phys.* **2004**, *95*, 3851–3879, doi:10.1063/1.1682673.
68. Cohen, A.J.; Mori-Sánchez, P.; Yang, W. Insights into Current Limitations of Density Functional Theory. *Science* **2008**, *321*, 792–794.
69. Heyd, J.; Scuseria, G.E.; Ernzerhof, M. Hybrid functionals based on a screened Coulomb potential. *J. Chem. Phys.* **2003**, *118*, 8207–8215.
70. Adamo, C.; Barone, V. Toward reliable density functional methods without adjustable parameters: The PBE0 model. *J. Chem. Phys.* **1999**, *110*, 6158–6170.

71. Dudarev, S.L.; Botton, G.A.; Savrasov, S.Y.; Humphreys, C.J.; Sutton, A.P. Electron-energy-loss spectra and the structural stability of nickel oxide: An LSDA+U study. *Phys. Rev. B* **1998**, *57*, 1505–1509.
72. Liechtenstein, A.I.; Anisimov, V.I.; Zaanen, J. Density-functional theory and strong interactions: Orbital ordering in Mott-Hubbard insulators. *Phys. Rev. B* **1995**, *52*, R5467–R5470.
73. Makov, G.; Payne, M.C. Periodic boundary conditions in ab initio calculations. *Phys. Rev. B* **1995**, *51*, 4014–4022.
74. Moss, T.S. The Interpretation of the Properties of Indium Antimonide. *Proc. Phys. Soc. Sect. B* **1954**, *67*, 775.
75. Burstein, E. Anomalous Optical Absorption Limit in InSb. *Phys. Rev.* **1954**, *93*, 632–633.
76. Vanpoucke, D.E.P.; Bultinck, P.; Cottenier, S.; Van Speybroeck, V.; Van Driessche, I. Aliovalent doping of CeO₂: DFT study of oxidation state and vacancy effects. *J. Mater. Chem. A* **2014**, *2*, 13723–13737.
77. Celotti, G.; Nobili, D.; Ostojia, P. Lattice parameter study of silicon uniformly doped with boron and phosphorus. *J. Mater. Sci.* **1974**, *9*, 821–828.
78. Denton, A.R.; Ashcroft, N.W. Vegard's law. *Phys. Rev. A* **1991**, *43*, 3161–3164.
79. Birch, F. Finite Elastic Strain of Cubic Crystals. *Phys. Rev.* **1947**, *71*, 809–824.
80. Murnaghan, F.D. The Compressibility of Media under Extreme Pressures. *Proc. Natl. Acad. Sci. USA* **1944**, *30*, 244–247.
81. Asahi, R.; Morikawa, T.; Ohwaki, T.; Aoki, K.; Taga, Y. Visible-Light Photocatalysis in Nitrogen-Doped Titanium Oxides. *Science* **2001**, *293*, 269–271.
82. Livraghi, S.; Paganini, M.C.; Giamello, E.; Selloni, A.; Di Valentin, C.; Pacchioni, G. Origin of Photoactivity of Nitrogen-Doped Titanium Dioxide under Visible Light. *J. Am. Chem. Soc.* **2006**, *128*, 15666–15671, doi:10.1021/ja064164c.
83. Di Valentin, C.; Pacchioni, G.; Selloni, A. Reduced and n-Type Doped TiO₂: Nature of Ti³⁺ Species. *J. Phys. Chem. C* **2009**, *113*, 20543–20552, doi:10.1021/jp9061797.
84. Kamisaka, H.; Adachi, T.; Yamashita, K. Theoretical study of the structure and optical properties of carbon-doped rutile and anatase titanium oxides. *J. Chem. Phys.* **2005**, *123*, 084704, doi:10.1063/1.2007630.
85. Di Valentin, C.; Pacchioni, G.; Selloni, A. Theory of Carbon Doping of Titanium Dioxide. *Chem. Mater.* **2005**, *17*, 6656–6665, doi:10.1021/cm051921h.
86. Liu, G.; Zhao, Y.; Sun, C.; Li, F.; Lu, G.; Cheng, H.M. Synergistic Effects of B/N Doping on the Visible-Light Photocatalytic Activity of Mesoporous TiO₂. *Angew. Chem. Int. Ed.* **2008**, *47*, 4516–4520.
87. Long, R.; English, N.J. First-Principles Calculation of Synergistic (N,P)-Codoping Effects on the Visible-Light Photocatalytic Activity of Anatase TiO₂. *J. Phys. Chem. C* **2010**, *114*, 11984–11990, doi:10.1021/jp100802r.
88. Long, R.; English, N.J. Synergistic Effects of Bi/S Codoping on Visible Light-Activated Anatase TiO₂ Photocatalysts from First Principles. *J. Phys. Chem. C* **2009**, *113*, 8373–8377, doi:10.1021/jp900589k.
89. Pelaez, M.; Nolan, N.T.; Pillai, S.C.; Seery, M.K.; Falaras, P.; Kontos, A.G.; Dunlop, P.S.; Hamilton, J.W.; Byrne, J.; O'Shea, K.; et al. A review on the visible light active titanium dioxide photocatalysts for environmental applications. *Appl. Catal. B Environ.* **2012**, *125*, 331–349.
90. Schneider, J.; Matsuoka, M.; Takeuchi, M.; Zhang, J.; Horiuchi, Y.; Anpo, M.; Bahnemann, D.W. Understanding TiO₂ Photocatalysis: Mechanisms and Materials. *Chem. Rev.* **2014**, *114*, 9919–9986, doi:10.1021/cr5001892.
91. Islam, S.Z.; Nagpure, S.; Kim, D.Y.; Rankin, S.E. Synthesis and Catalytic Applications of Non-Metal Doped Mesoporous Titania. *Inorganics* **2017**, *5*, 15.
92. Meng, X.Y.; Qin, G.W.; Li, S.; Wen, X.H.; Ren, Y.P.; Pei, W.L.; Zuo, L. Enhanced photoelectrochemical activity for Cu and Ti doped hematite: The first principles calculations. *Appl. Phys. Lett.* **2012**, *98*, 112104.
93. Liang, W.Y. Excitons. *Phys. Educ.* **1970**, *5*, 226.
94. Dember, H. Über eine photoelektronische Kraft in Kupferoxydul-Kristallen (Photoelectric E.M.F. in Cuprous-Oxide Crystals). *Z. Phys.* **1931**, *32*, 554.
95. Sze, S.M. *Semiconductor Devices, Physics and Technology*; Wiley: Hoboken, NJ, USA, 1985.
96. Grätzel, M. Photoelectrochemical cells. *Nature* **2001**, *414*, 338–344.
97. Ikeda, K.; Umezawa, H.; Ramanujam, K.; ichi Shikata, S. Thermally Stable Schottky Barrier Diode by Ru/Diamond. *Appl. Phys. Express* **2009**, *2*, 011202.
98. Kwon, S.; Lee, S.J.; Kim, S.M.; Lee, Y.; Song, H.; Park, J.Y. Probing the nanoscale Schottky barrier of metal/semiconductor interfaces of Pt/CdSe/Pt nanodumbbells by conductive-probe atomic force microscopy. *Nanoscale* **2015**, *7*, 12297–12301.

99. Durcan, C.A.; Balsano, R.; LaBella, V.P. Nanoscale mapping of the W/Si(001) Schottky barrier. *J. Appl. Phys.* **2014**, *116*, 023705.
100. Durcan, C.A.; Balsano, R.; LaBella, V.P. Time dependent changes in Schottky barrier mapping of the W/Si(001) interface utilizing ballistic electron emission microscopy. *J. Appl. Phys.* **2015**, *117*, 245306.
101. Tung, R.T. Electron transport at metal-semiconductor interfaces: General theory. *Phys. Rev. B* **1992**, *45*, 13509–13523.
102. Tung, R.T. Recent advances in Schottky barrier concepts. *Mater. Sci. Eng. R Rep.* **2001**, *35*, 1–138.
103. Tung, R.T. The physics and chemistry of the Schottky barrier height. *Appl. Phys. Rev.* **2014**, *1*, 011304.
104. Jiao, Y.; Hellman, A.; Fang, Y.; Gao, S.; Käll, M. Schottky barrier formation and band bending revealed by first-principles calculations. *Sci. Rep.* **2015**, *5*, 11374.
105. Austin, I.; Mott, N. Polarons in crystalline and non-crystalline materials. *Adv. Phys.* **1969**, *18*, 41–102.
106. Shluger, A.L.; Stoneham, A.M. Small polarons in real crystals: Concepts and problems. *J. Phys. Condens. Matter* **1993**, *5*, 3049.
107. Bosman, A.; van Daal, H. Small-polaron versus band conduction in some transition-metal oxides. *Adv. Phys.* **1970**, *19*, 1–117.
108. Marcus, R.A. On the Theory of Oxidation—Reduction Reactions Involving Electron Transfer. I. *J. Chem. Phys.* **1956**, *24*, 966–978.
109. Hellman, A.; Razaznejad, B.; Lundqvist, B.I. Potential-energy surfaces for excited states in extended systems. *J. Chem. Phys.* **2004**, *120*, 4593–4602.
110. Gavnholt, J.; Olsen, T.; Englund, M.; Schiøtz, J. Δ Self-consistent field method to obtain potential energy surfaces of excited molecules on surfaces. *Phys. Rev. B* **2008**, *78*, 075441.
111. Zawadzki, P.; Laursen, A.B.; Jacobsen, K.W.; Dahl, S.; Rossmeisl, J. Oxidative trends of TiO₂-hole trapping at anatase and rutile surfaces. *Energy Environ. Sci.* **2012**, *5*, 9866–9869.
112. Lany, S.; Zunger, A. Polaronic hole localization and multiple hole binding of acceptors in oxide wide-gap semiconductors. *Phys. Rev. B* **2009**, *80*, 085202.
113. Alexandrov, V.; Neumann, A.; Scherer, M.M.; Rosso, K.M. Electron Exchange and Conduction in Nontronite from First-Principles. *J. Phys. Chem. C* **2013**, *117*, 2032–2040.
114. Maxisch, T.; Zhou, F.; Ceder, G. *Ab initio* study of the migration of small polarons in olivine Li_xFePO₄ and their association with lithium ions and vacancies. *Phys. Rev. B* **2006**, *73*, 104301.
115. Chen, H.; Umezawa, N. Hole localization, migration, and the formation of peroxide anion in perovskite SrTiO₃. *Phys. Rev. B* **2014**, *90*, 035202.
116. Carvalho, A.; Alkauskas, A.; Pasquarello, A.; Tagantsev, A.K.; Setter, N. A hybrid density functional study of lithium in ZnO: Stability, ionization levels, and diffusion. *Phys. Rev. B* **2009**, *80*, 195205.
117. Zawadzki, P.; Jacobsen, K.W.; Rossmeisl, J. Electronic hole localization in rutile and anatase TiO₂-Self-interaction correction in Δ -SCF {DFT}. *Chem. Phys. Lett.* **2011**, *506*, 42–45.
118. Deskins, N.A.; Rousseau, R.; Dupuis, M. Localized Electronic States from Surface Hydroxyls and Polarons in TiO₂(110). *J. Phys. Chem. C* **2009**, *113*, 14583–14586.
119. Deskins, N.A.; Dupuis, M. Intrinsic Hole Migration Rates in TiO₂ from Density Functional Theory. *J. Phys. Chem. C* **2009**, *113*, 346–358.
120. Marcus, R.A. Electron transfer reactions in chemistry. Theory and experiment. *Rev. Mod. Phys.* **1993**, *65*, 599–610.
121. Holstein, T. Studies of Polaron Motion: Part I. The Molecular-Crystal Model. *Ann. Phys.* **2000**, *8*, 706–724.
122. Holstein, T. Studies of Polaron Motion: Part II. The “Small” Polaron. *Ann. Phys.* **2000**, *281*, 725–773.
123. Di Valentin, C.; Pacchioni, G.; Selloni, A. Electronic Structure of Defect States in Hydroxylated and Reduced Rutile TiO₂(110) Surfaces. *Phys. Rev. Lett.* **2006**, *97*, 166803.
124. Hurum, D.C.; Agrios, A.G.; Gray, K.A.; Rajh, T.; Thurnauer, M.C. Explaining the Enhanced Photocatalytic Activity of Degussa P25 Mixed-Phase TiO₂ Using EPR. *J. Phys. Chem. B* **2003**, *107*, 4545–4549.
125. Ji, Y.; Wang, B.; Luo, Y. Location of Trapped Hole on Rutile-TiO₂(110) Surface and Its Role in Water Oxidation. *J. Phys. Chem. C* **2012**, *116*, 7863–7866.
126. Kleiman-Shwarsstein, A.; Huda, M.N.; Walsh, A.; Yan, Y.; Stucky, G.D.; Hu, Y.S.; Al-Jassim, M.M.; McFarland, E.W. Electrodeposited Aluminum-Doped α -Fe₂O₃ Photoelectrodes: Experiment and Theory. *Chem. Mater.* **2010**, *22*, 510–517.
127. Liao, P.; Carter, E.A. Hole transport in pure and doped hematite. *J. Appl. Phys.* **2012**, *112*, 013701.

128. Adelstein, N.; Neaton, J.B.; Asta, M.; De Jonghe, L.C. Density functional theory based calculation of small-polaron mobility in hematite. *Phys. Rev. B* **2014**, *89*, 245115.
129. Pacchioni, G. Modeling doped and defective oxides in catalysis with density functional theory methods: Room for improvements. *J. Chem. Phys.* **2008**, *128*, 182505.
130. Shluger, A.L.; McKenna, K.P.; Sushko, P.V.; Ramo, D.M.; Kimmel, A.V. Modelling of electron and hole trapping in oxides. *Model. Simul. Mater. Sci. Eng.* **2009**, *17*, 084004.
131. Zou, Z.; Ye, J.; Sayama, K.; Arakawa, H. Direct splitting of water under visible light irradiation with an oxide semiconductor photocatalyst. *Nature* **2001**, *414*, 625–627.
132. Mahalingam, S.; Abdullah, H. Electron transport study of indium oxide as photoanode in DSSCs: A review. *Renew. Sustain. Energy Rev.* **2016**, *63*, 245–255.
133. Frank, A.J.; Kopidakis, N.; van de Lagemaat, J. Electrons in nanostructured TiO₂ solar cells: Transport, recombination and photovoltaic properties. *Coord. Chem. Rev.* **2004**, *248*, 1165–1179.
134. Riss, A.; Elser, M.J.; Bernardi, J.; Diwald, O. Stability and Photoelectronic Properties of Layered Titanate Nanostructures. *J. Am. Chem. Soc.* **2009**, *131*, 6198–6206, doi:10.1021/ja810109g.
135. Xia, Y.; Yang, P.; Sun, Y.; Wu, Y.; Mayers, B.; Gates, B.; Yin, Y.; Kim, F.; Yan, H. One-Dimensional Nanostructures: Synthesis, Characterization, and Applications. *Adv. Mater.* **2003**, *15*, 353–389.
136. Anta, J.A.; Nelson, J.; Quirke, N. Charge transport model for disordered materials: Application to sensitized TiO₂. *Phys. Rev. B* **2002**, *65*, 125324.
137. Göpel, W.; Rocker, G.; Feierabend, R. Intrinsic defects of TiO₂(110): Interaction with chemisorbed O₂, H₂, CO, and CO₂. *Phys. Rev. B* **1983**, *28*, 3427–3438.
138. Wickman, B.; Bastos Fanta, A.; Burrows, A.; Hellman, A.; Wagner, J.B.; Iandolo, B. Iron Oxide Films Prepared by Rapid Thermal Processing for Solar Energy Conversion. *Sci. Rep.* **2017**, *7*, 40500.
139. Xu, J.; Wang, Z.; Li, W.; Zhang, X.; He, D.; Xiao, X. Ag Nanoparticles Located on Three-Dimensional Pine Tree-Like Hierarchical TiO₂ Nanotube Array Films as High-Efficiency Plasmonic Photocatalysts. *Nanoscale Res. Lett.* **2017**, *12*, 54.
140. Antony, A.C.; Akhade, S.A.; Liang, T.; Janik, M.J.; Maranas, J.K.; Sinnott, S.B. Simulating an Applied Voltage in Molecular Dynamics Using Charge Optimized Many Body (COMB3) Potentials. *ECS Trans.* **2015**, *69*, 103–105.
141. Van de Lagemaat, J.; Park, N.G.; Frank, A.J. Influence of Electrical Potential Distribution, Charge Transport, and Recombination on the Photopotential and Photocurrent Conversion Efficiency of Dye-Sensitized Nanocrystalline TiO₂ Solar Cells: A Study by Electrical Impedance and Optical Modulation Techniques. *J. Phys. Chem. B* **2000**, *104*, 2044–2052, doi:10.1021/jp993172v.
142. De Jongh, P.E.; Vanmaekelbergh, D. Trap-Limited Electronic Transport in Assemblies of Nanometer-Size TiO₂ Particles. *Phys. Rev. Lett.* **1996**, *77*, 3427–3430.
143. Vanmaekelbergh, D.; de Jongh, P.E. Electron transport in disordered semiconductors studied by a small harmonic modulation of the steady state. *Phys. Rev. B* **2000**, *61*, 4699–4704.
144. Anderson, A.B.; Albu, T.V. Ab Initio Determination of Reversible Potentials and Activation Energies for Outer-Sphere Oxygen Reduction to Water and the Reverse Oxidation Reaction. *J. Am. Chem. Soc.* **1999**, *121*, 11855–11863.
145. Anderson, A.B.; Neshev, N.M.; Sidik, R.A.; Shiller, P. Mechanism for the electrooxidation of water to {OH} and O bonded to platinum: Quantum chemical theory. *Electrochim. Acta* **2002**, *47*, 2999–3008.
146. Jinnouchi, R.; Anderson, A.B. Aqueous and Surface Redox Potentials from Self-Consistently Determined Gibbs Energies. *J. Phys. Chem. C* **2008**, *112*, 8747–8750.
147. Anderson, A.B. Insights into electrocatalysis. *Phys. Chem. Chem. Phys.* **2012**, *14*, 1330–1338.
148. Anderson, A.B. Theory at the electrochemical interface: Reversible potentials and potential-dependent activation energies. *Electrochim. Acta* **2003**, *48*, 3743–3749.
149. Anderson, A.B. Theories for Predicting Reversible Potentials of Reactions on Electrode Surfaces from Internal and Gibbs Energies: Applications to ORR. *ECS Trans.* **2010**, *28*, 1–17.
150. Taylor, C.D.; Kelly, R.G.; Neurock, M. A first-principles analysis of the chemisorption of hydroxide on copper under electrochemical conditions: A probe of the electronic interactions that control chemisorption at the electrochemical interface. *J. Electroanal. Chem.* **2007**, *607*, 167–174.
151. Taylor, C.; Kelly, R.G.; Neurock, M. First-Principles Calculations of the Electrochemical Reactions of Water at an Immersed Ni (111)/H₂O Interface. *J. Electrochem. Soc.* **2006**, *153*, E207–E214.

152. Taylor, C.D.; Kelly, R.G.; Neurock, M. First-Principles Prediction of Equilibrium Potentials for Water Activation by a Series of Metals. *J. Electrochem. Soc.* **2007**, *154*, F217–F221.
153. Janik, M.J.; Taylor, C.D.; Neurock, M. First-Principles Analysis of the Initial Electroreduction Steps of Oxygen over Pt(111). *J. Electrochem. Soc.* **2009**, *156*, B126–B135.
154. Taylor, C.; Kelly, R.G.; Neurock, M. Theoretical Analysis of the Nature of Hydrogen at the Electrochemical Interface Between Water and a Ni(111) Single-Crystal Electrode. *J. Electrochem. Soc.* **2007**, *154*, F55–F64.
155. Skúlason, E.; Tripkovic, V.; Björketun, M.E.; Gudmundsdóttir, S.; Karlberg, G.; Rossmeisl, J.; Bligaard, T.; Jónsson, H.; Nørskov, J.K. Modeling the Electrochemical Hydrogen Oxidation and Evolution Reactions on the Basis of Density Functional Theory Calculations. *J. Phys. Chem. C* **2010**, *114*, 18182–18197.
156. Bondarenko, A.S.; Stephens, I.E.L.; Hansen, H.A.; Pérez-Alonso, F.J.; Tripkovic, V.; Johansson, T.P.; Rossmeisl, J.; Nørskov, J.K.; Chorkendorff, I. The Pt(111)/Electrolyte Interface under Oxygen Reduction Reaction Conditions: An Electrochemical Impedance Spectroscopy Study. *Langmuir* **2011**, *27*, 2058–2066.
157. Nørskov, J.K.; Rossmeisl, J.; Logadottir, A.; Lindqvist, L.; Kitchin, J.R.; Bligaard, T.; Jónsson, H. Origin of the Overpotential for Oxygen Reduction at a Fuel-Cell Cathode. *J. Phys. Chem. B* **2004**, *108*, 17886–17892.
158. Rossmeisl, J.; Logadottir, A.; Nørskov, J. Electrolysis of water on (oxidized) metal surfaces. *Chem. Phys.* **2005**, *319*, 178–184.
159. Rossmeisl, J.; Nørskov, J.K.; Taylor, C.D.; Janik, M.J.; Neurock, M. Calculated Phase Diagrams for the Electrochemical Oxidation and Reduction of Water over Pt(111). *J. Phys. Chem. B* **2006**, *110*, 21833–21839.
160. Greeley, J.; Rossmeisl, J.; Hellman, A.; Nørskov, J.K. Theoretical Trends in Particle Size Effects for the Oxygen Reduction Reaction. *Z. Phys. Chem.* **2007**, *221*, 1209–1220.
161. Rossmeisl, J.; Qu, Z.W.; Zhu, H.; Kroes, G.J.; Nørskov, J. Electrolysis of water on oxide surfaces. *J. Electroanal. Chem.* **2007**, *607*, 83–89.
162. Nielsen, M.; Björketun, M.E.; Hansen, M.H.; Rossmeisl, J. Towards first principles modeling of electrochemical electrode–electrolyte interfaces. *Surf. Sci.* **2015**, *613*, 2–7.
163. Valdés, Á.; Qu, Z.-W.; Kroes, G.-J.; Rossmeisl, J.; Nørskov, J.K. Oxidation and Photo-Oxidation of Water on TiO₂ Surface. *J. Phys. Chem. C* **2008**, *112*, 9872–9879.
164. Valdés, Á.; Kroes, G.J. First principles study of the photo-oxidation of water on tungsten trioxide (WO₃). *J. Chem. Phys.* **2009**, *130*, 114701.
165. Valdés, Á.; Kroes, G.J. Cluster Study of the Photo-Oxidation of Water on Rutile Titanium Dioxide (TiO₂). *J. Phys. Chem. C* **2010**, *114*, 1701–1708.
166. Calle-Vallejo, F.; Koper, M.T. First-principles computational electrochemistry: Achievements and challenges. *Electrochim. Acta* **2012**, *84*, 3–11.
167. Karlberg, G.S.; Rossmeisl, J.; Nørskov, J.K. Estimations of electric field effects on the oxygen reduction reaction based on the density functional theory. *Phys. Chem. Chem. Phys.* **2007**, *9*, 5158–5161.
168. Fenter, P.; Sturchio, N.C. Mineral-water interfacial structures revealed by synchrotron X-ray scattering. *Prog. Surf. Sci.* **2004**, *77*, 171–258.
169. Sato, N. *Electrochemistry at Metal and Semiconductor Electrodes*; Elsevier: Oxford, UK, 1998.
170. Björneholm, O.; Hansen, M.H.; Hodgson, A.; Liu, L.M.; Limmer, D.T.; Michaelides, A.; Pedevilla, P.; Rossmeisl, J.; Shen, H.; Tocci, G.; et al. Simulating an Applied Voltage in Molecular Dynamics Using Charge Optimized Many Body (COMB3) Potentials. *Chem. Rev.* **2016**, *116*, 7698–7726.
171. Skúlason, E.; Karlberg, G.S.; Rossmeisl, J.; Bligaard, T.; Greeley, J.; Jónsson, H.; Nørskov, J.K. Density functional theory calculations for the hydrogen evolution reaction in an electrochemical double layer on the Pt(111) electrode. *Phys. Chem. Chem. Phys.* **2007**, *9*, 3241–3250.
172. Yeh, K.Y.; Wasileski, S.A.; Janik, M.J. Electronic structure models of oxygen adsorption at the solvated, electrified Pt(111) interface. *Phys. Chem. Chem. Phys.* **2009**, *11*, 10108–10117.
173. Yeh, K.Y.; Janik, M.J.; Maranas, J.K. Molecular dynamics simulations of an electrified water/Pt(111) interface using point charge dissociative water. *Electrochim. Acta* **2013**, *101*, 308–325.
174. Hansen, M.H.; Jin, C.; Thygesen, K.S.; Rossmeisl, J. Finite Bias Calculations to Model Interface Dipoles in Electrochemical Cells at the Atomic Scale. *J. Phys. Chem. C* **2016**, *120*, 13485–13491.
175. Zhang, C.; Sprik, M. Finite field methods for the supercell modeling of charged insulator/electrolyte interfaces. *Phys. Rev. B* **2016**, *94*, 245309.

176. Russo, D.; Teixeira, J.; Kneller, L.; Copley, J.R.D.; Ollivier, J.; Perticaroli, S.; Pellegrini, E.; Gonzalez, M.A. Vibrational Density of States of Hydration Water at Biomolecular Sites: Hydrophobicity Promotes Low Density Amorphous Ice Behavior. *J. Am. Chem. Soc.* **2011**, *133*, 4882–4888, doi:10.1021/ja109610f.
177. Kumar, N.; Neogi, S.; Kent, P.R.C.; Bandura, A.V.; Kubicki, J.D.; Wesolowski, D.J.; Cole, D.; Sofo, J.O. Hydrogen Bonds and Vibrations of Water on (110) Rutile. *J. Phys. Chem. C* **2009**, *113*, 13732–13740, doi:10.1021/jp901665e.
178. English, N.J.; Kavathekar, R.S.; MacElroy, J. Hydrogen bond dynamical properties of adsorbed liquid water monolayers with various TiO₂ interfaces. *Mol. Phys.* **2012**, *110*, 2919–2925, doi:10.1080/00268976.2012.683888.
179. Kavathekar, R.S.; Dev, P.; English, N.J.; MacElroy, J. Molecular dynamics study of water in contact with the TiO₂ rutile-110, 100, 101, 001 and anatase-101, 001 surface. *Mol. Phys.* **2011**, *109*, 1649–1656, doi:10.1080/00268976.2011.582051.
180. Iandolo, B.; Hellman, A. The Role of Surface States in the Oxygen Evolution Reaction on Hematite. *Angew. Chem. Int. Ed.* **2014**, *53*, 13404–13408.
181. Hellman, A.; Pala, R.G.S. First-Principles Study of Photoinduced Water-Splitting on Fe₂O₃. *J. Phys. Chem. C* **2011**, *115*, 12901–12907.
182. Hellman, A.; Iandolo, B.; Wickman, B.; Grönbeck, H.; Baltusaitis, J. Electro-oxidation of water on hematite: Effects of surface termination and oxygen vacancies investigated by first-principles. *Surf. Sci.* **2015**, *640*, 45–49.
183. Hansen, H.A.; Rossmeisl, J.; Nørskov, J.K. Surface Pourbaix diagrams and oxygen reduction activity of Pt, Ag and Ni(111) surfaces studied by DFT. *Phys. Chem. Chem. Phys.* **2008**, *10*, 3722–3730.
184. Persson, K.A.; Waldwick, B.; Lazic, P.; Ceder, G. Prediction of solid-aqueous equilibria: Scheme to combine first-principles calculations of solids with experimental aqueous states. *Phys. Rev. B* **2012**, *85*, 235438.
185. Todorova, M.; Neugebauer, J. Extending the Concept of Defect Chemistry from Semiconductor Physics to Electrochemistry. *Phys. Rev. Appl.* **2014**, *1*, 014001.
186. Huang, L.F.; Rondinelli, J.M. Electrochemical phase diagrams for Ti oxides from density functional calculations. *Phys. Rev. B* **2015**, *92*, 245126.
187. Zeng, Z.; Chan, M.K.Y.; Zhao, Z.J.; Kubal, J.; Fan, D.; Greeley, J. Towards First Principles-Based Prediction of Highly Accurate Electrochemical Pourbaix Diagrams. *J. Phys. Chem. C* **2015**, *119*, 18177–18187.
188. Ulissi, Z.W.; Singh, A.R.; Tsai, C.; Nørskov, J.K.; Todorova, M.; Neugebauer, J. Automated Discovery and Construction of Surface Phase Diagrams Using Machine Learning. *J. Phys. Chem. Lett.* **2016**, *7*, 3931–3935.
189. Pourbaix, M. *Atlas of Electrochemical Equilibria in Aqueous Solutions*, 2nd ed.; National Association of Corrosion Engineers: Houston, TX, USA, 1974.
190. Nguyen, M.T.; Piccinin, S.; Seriani, N.; Gebauer, R. Photo-Oxidation of Water on Defective Hematite(0001). *ACS Catal.* **2015**, *5*, 715–721.
191. Nørskov, J.K.; Bligaard, T.; Logadottir, A.; Bahn, S.; Hansen, L.B.; Bollinger, M.; Bengaard, H.; Hammer, B.; Slijivancanin, Z.; Mavrikakis, M.; et al. Universality in Heterogeneous Catalysis. *J. Catal.* **2002**, *209*, 275.
192. Nguyen, M.T.; Seriani, N.; Gebauer, R. Water adsorption and dissociation on α -Fe₂O₃(0001): PBE+U calculations. *J. Chem. Phys.* **2013**, *138*, 194709.
193. Toroker, M.C. Theoretical Insights into the Mechanism of Water Oxidation on Nonstoichiometric and Titanium-Doped Fe₂O₃(0001). *J. Phys. Chem. C* **2014**, *118*, 23162–23167.
194. Zeng, Z.; Hansen, M.H.; Greeley, J.P.; Rossmeisl, J.; Björketun, M.E. Ab Initio Thermodynamic Modeling of Electrified Metal–Oxide Interfaces: Consistent Treatment of Electronic and Ionic Chemical Potentials. *J. Phys. Chem. C* **2014**, *118*, 22663–22671.
195. Chan, K.; Nørskov, J.K. Electrochemical Barriers Made Simple. *J. Phys. Chem. Lett.* **2015**, *6*, 2663–2668.
196. Abild-Pedersen, F.; Greeley, J.; Studt, F.; Rossmeisl, J.; Munter, T.R.; Moses, P.G.; Skúlason, E.; Bligaard, T.; Nørskov, J.K. Scaling Properties of Adsorption Energies for Hydrogen-Containing Molecules on Transition-Metal Surfaces. *Phys. Rev. Lett.* **2007**, *99*, 016105.
197. Bligaard, T.; Nørskov, J.; Dahl, S.; Matthiesen, J.; Christensen, C.; Sehested, J. The Brønsted–Evans–Polanyi relation and the volcano curve in heterogeneous catalysis. *J. Catal.* **2004**, *224*, 206–217.
198. Nørskov, J.K.; Bligaard, T.; Rossmeisl, J.; Christensen, C.H. Towards the computational design of solid catalysts. *Nat. Chem.* **2009**, *1*, 37–46.

199. Man, I.C.; Su, H.Y.; Calle-Vallejo, F.; Hansen, H.A.; Martínez, J.I.; Inoglu, N.G.; Kitchin, J.; Jaramillo, T.F.; Nørskov, J.K.; Rossmeisl, J. Universality in Oxygen Evolution Electrocatalysis on Oxide Surfaces. *ChemCatChem* **2011**, *3*, 1159–1165.
200. García-Mota, M.; Vojvodic, A.; Metiu, H.; Man, I.C.; Su, H.Y.; Rossmeisl, J.; Nørskov, J.K. Tailoring the Activity for Oxygen Evolution Electrocatalysis on Rutile TiO₂(110) by Transition-Metal Substitution. *ChemCatChem* **2011**, *3*, 1607–1611.
201. Montoya, J.H.; Garcia-Mota, M.; Nørskov, J.K.; Vojvodic, A. Theoretical evaluation of the surface electrochemistry of perovskites with promising photon absorption properties for solar water splitting. *Phys. Chem. Chem. Phys.* **2015**, *17*, 2634–2640.
202. Calle-Vallejo, F.; Martinez, J.I.; Rossmeisl, J. Density functional studies of functionalized graphitic materials with late transition metals for oxygen reduction reactions. *Phys. Chem. Chem. Phys.* **2011**, *13*, 15639–15643.
203. Dogutan, D.K.; Bediako, D.K.; Teets, T.S.; Schwalbe, M.; Nocera, D.G. Efficient Synthesis of Hangman Porphyrins. *Org. Lett.* **2010**, *12*, 1036–1039.
204. McGuire R., Jr.; Dogutan, D.K.; Teets, T.S.; Suntivich, J.; Shao-Horn, Y.; Nocera, D.G. Oxygen reduction reactivity of cobalt(II) hangman porphyrins. *Chem. Sci.* **2010**, *1*, 411–414.
205. Rosenthal, J.; Nocera, D. Oxygen activation chemistry of Pacman and Hangman porphyrin architectures based on xanthene and dibenzofuran spacers. In *Progress in Inorganic Chemistry*; Wiley: Hoboken, NJ, USA, 2007; Volume 55, pp. 483–544.
206. Dogutan, D.K.; Stoian, S.A.; McGuire, R.; Schwalbe, M.; Teets, T.S.; Nocera, D.G. Hangman Corroles: Efficient Synthesis and Oxygen Reaction Chemistry. *J. Am. Chem. Soc.* **2011**, *133*, 131–140.
207. Chang, C.J.; Chng, L.L.; Nocera, D.G. Proton-Coupled O–O Activation on a Redox Platform Bearing a Hydrogen-Bonding Scaffold. *J. Am. Chem. Soc.* **2003**, *125*, 1866–1876.
208. Baran, J.D.; Grönbeck, H.; Hellman, A. Analysis of Porphyrines as Catalysts for Electrochemical Reduction of O₂ and Oxidation of H₂O. *J. Am. Chem. Soc.* **2014**, *136*, 1320–1326.
209. Que, L.; Tolman, W.B. Biologically inspired oxidation catalysis. *Nature* **2008**, *455*, 333–340.
210. Shook, R.L.; Borovik, A.S. Role of the Secondary Coordination Sphere in Metal-Mediated Dioxygen Activation. *Inorg. Chem.* **2010**, *49*, 3646–3660.
211. Wang, B. Electronic Structure and Optical Properties of Solar Energy Materials. Ph.D. Dissertation, Royal Institute of Technology, KTH, Stockholm, Sweden, 2014.
212. Martin, R.M. *Electronic Structure : Basic Theory and Practical Methods*; Cambridge University Press: Cambridge, UK, 2004.
213. Kohn, W.; Sham, L.J. Self-Consistent Equations Including Exchange and Correlation Effects. *Phys. Rev.* **1965**, *140*, A1133–A1138.
214. Slater, J.C. A Simplification of the Hartree-Fock Method. *Phys. Rev.* **1951**, *81*, 385–390.
215. Ceperley, D.M.; Alder, B.J. Ground State of the Electron Gas by a Stochastic Method. *Phys. Rev. Lett.* **1980**, *45*, 566–569.
216. Csonka, G.I.; Perdew, J.P.; Ruzsinszky, A.; Philipsen, P.H.T.; Lebègue, S.; Paier, J.; Vydrov, O.A.; Ángyán, J.G. Assessing the performance of recent density functionals for bulk solids. *Phys. Rev. B* **2009**, *79*, 155107.
217. Staroverov, V.N.; Scuseria, G.E.; Tao, J.; Perdew, J.P. Tests of a ladder of density functionals for bulk solids and surfaces. *Phys. Rev. B* **2004**, *69*, 075102.
218. Perdew, J.P. Accurate Density Functional for the Energy: Real-Space Cutoff of the Gradient Expansion for the Exchange Hole. *Phys. Rev. Lett.* **1985**, *55*, 1665–1668.
219. Langreth, D.C.; Mehl, M.J. Easily Implementable Nonlocal Exchange-Correlation Energy Functional. *Phys. Rev. Lett.* **1981**, *47*, 446–450.
220. Gunnarson, O.; Lundqvist, B.; Lundqvist, S. Screening in a spin-polarized electron liquid. *Solid State Commun.* **1972**, *11*, 149–153.
221. Beck, A.D. Density-functional exchange-energy approximation with correct asymptotic behavior. *Phys. Rev. A* **1988**, *38*, 3098–3100.
222. Perdew, J.P.; Wang, Y. Accurate and simple analytic representation of the electron-gas correlation energy. *Phys. Rev. B* **1992**, *45*, 13244–13249.
223. Perdew, J.P.; Burke, K.; Ernzerhof, M. Generalized Gradient Approximation Made Simple. *Phys. Rev. Lett.* **1996**, *77*, 3865–3868.

- 224. Armiento, R.; Mattsson, A.E. Functional designed to include surface effects in self-consistent density functional theory. *Phys. Rev. B* **2005**, *72*, 085108.
- 225. Tao, J.M.; Perdew, J.P.; Staroverov, V.N.; Scuseria, G.E. Climbing the Density Functional Ladder: Nonempirical Meta? Generalized Gradient Approximation Designed for Molecules and Solids. *Phys. Rev. Lett.* **2003**, *91*, 146401.
- 226. Perdew, J.P.; Ruzsinszky, A.; Csonka, G.I.; Constantin, L.A.; Sun, J. Workhorse Semilocal Density Functional for Condensed Matter Physics and Quantum Chemistry. *Phys. Rev. Lett.* **2009**, *103*, 026403.
- 227. Zhao, Y.; Truhlar, D.G. Exploring the Limit of Accuracy of the Global Hybrid Meta Density Functional for Main-Group Thermochemistry, Kinetics, and Noncovalent Interactions. *J. Chem. Theory Comput.* **2008**, *4*, 1849–1868.
- 228. Becke, A.D. A new mixing of Hartree Fock and local density functional theories. *J. Chem. Phys.* **1993**, *98*, 1372–1377.
- 229. Kim, K.; Jordan, K.D. Comparison of Density Functional and MP2 Calculations on the Water Monomer and Dimer. *J. Phys. Chem.* **1994**, *98*, 10089–10094.
- 230. Stephens, P.J.; Devlin, F.J.; Chabalowski, C.F.; Frisch, M.J. Ab Initio Calculation of Vibrational Absorption and Circular Dichroism Spectra Using Density Functional Force Fields. *J. Phys. Chem.* **1994**, *98*, 11623–11627.
- 231. Becke, A.D. Density functional thermochemistry. III. The role of exact exchange. *J. Chem. Phys.* **1993**, *98*, 5648–5652.



© 2017 by the authors. Licensee MDPI, Basel, Switzerland. This article is an open access article distributed under the terms and conditions of the Creative Commons Attribution (CC BY) license (<http://creativecommons.org/licenses/by/4.0/>).